Thermomechanical modelling of lithospheric slab tearing and its topographic response. Application to the Gibraltar Arc.

Kittiphon Boonma[1,2], Daniel Garcia-Castellanos[1], Ivone Jiménez-Munt[1], Taras Gerya[3]

[1] GeoSciences Barcelona, Geo3BCN-CSIC, Lluís Solé i Sabaris, s/n, 08028 Barcelona, Spain

[2] Departament de Dinàmica de la Terra i de l'Oceà, Universitat de Barcelona, Spain

[3] Department of Geophysics, EDRW, ETH Zürich

Correspondence author: Kittiphon Boonma (`kittiphon.b@gmail.com`)

Key points:

- An oblique initial passive margin promotes a laterally diachronous continental convergence, which leads to slab tearing.
- The viscosity of the sublithospheric mantle and the amount of shortening prior tearing are the key controls on the slab-tearing dynamics.
- Our obtained surface uplift rates of 0.23–2.16 mm/yr for the overriding plate are compatible with the onset of Messinian Salinity Crisis.

Abstract

Lithospheric slab tearing, the process by which a subducted lithospheric plate is torn apart and sinks into the Earth's mantle, has been proposed as a cause for significant surface vertical motions. However, little is known about the mechanisms that help initiate slab tearing and the consequential topographic changes. This study aims to explore this process by means of 3D thermo-mechanical modelling. We use the Gibraltar Arc region (Betics Cordillera) as a reference scenario of continental collision where such tearing-uplift interaction has been proposed. Our results suggest that the obliquity of the continental passive margin (relative to the trench axis) is a major influence on the initiation of slab tearing because it promotes a laterally diachronous continental collision, which leads to earlier tearing inception in one end of the slab. As a result of this, the model results predict an east-to-west slab tearing (tearing velocity 37.6–67.6 cm/yr with the lower-mantle viscosity of up to 1e+22 Pa $\cdot$ s). While the fast slab tearing (<2 Myr over 600 km wide slab) and the lack of arcuate slab in our models limit a direct comparison with the Western Mediterranean, this approach provides a new insight into the link between slab tearing in the mantle and surface uplift. Our models yield uplift rates of 0.23–2.16 mm/yr in response to slab tearing. This range is compatible with the uplift rate needed to achieve an equilibrium between seaway-uplift and seaway-erosion, which could have led to the closure of marine gateways during the onset of the Messinian Salinity Crisis.

Plain Language Summary

As a tectonic plate sinks during plate collision and 'subduction', its properties change and it becomes weaker and denser so that the sinking portion can start to tear off. Understanding the tearing process and its link to the Earth's surface could help us better understand the tectonic evolution. This study explores what could cause the plates to tear apart and what are the after-effects of this plate tearing. Could the plate tearing (occurring deep within the Earth's interior) be the cause of crustal surface uplift (shallow process)? If so, how much? We used 3D computational model to study what goes on during the plate tearing. We found that when a subduction zone reaches a stationary continental plate that makes an oblique angle with the subduction zone, it increases a chance of the sinking plate tearing off. The horizontal tearing rate in our model was between 37-68 cm/yr. The plate tearing in our model caused the Earth's surface to uplift at the rate of up to 2 mm/yr, within the range that could have caused the Mediterranean Sea to disconnect from the Atlantic Ocean, just under 6 million years ago.

Introduction

The perception that some areas of the continental crust have been risen at rates that cannot be explained by crustal thickening or fault activity alone, has pointed the need to other epeirogenic surface uplift mechanisms (England and Molnar, 1990) including dynamic topography or isostatic responses to mass motions. Slab breakoff is among the deep-seated mechanisms invoked to justify the long-wavelength, high rates of surface uplift observed in some continental collision settings (Davies and von Blanckenburg, 1995; Spakman et al., 1988; Van Der Meulen et al. , 1998; Wortel and Spakman, 1992;2000). Uplift is in such scenarios purportedly driven by the cancellation of the negative buoyancy force, the same force that drives slab pull and subduction (e.g. Garcia-Castellanos et al., 2000; Conrad and Lithgow-Bertelloni, 2002; Billen, 2008; Boonma et al., 2019; Jiménez-Munt et al., 2019). Slab breakoff is a process happening at depth within the mantle consisting of the detachment of a subducted oceanic lithospheric slab from the more buoyant continental lithosphere during a continental collision. The concept of slab breakoff, as inferred from seismic tomography, was first proposed to be involved in the geodynamical evolution of the Mediterranean by Spakman et al. (1988) and Wortel and Spakman (1992). Slab breakoff was then used to explain post-collisional magmatism and exhumation of high-pressure rocks in the European Alps by Davies and von Blanckenburg (1995). Garzanti et al. (2018), and references therein, gave a comprehensive global overview of where slab breakoff has been invoked to explain changes in plate kinematics and tectonic deformation, e.g. the Alps (Spakman et al., 1988; Wortel and Spakman, 1992; Davies and von Blanckenburg, 1995; Sinclair, 1997; Fox et al., 2015), the Mediterranean region (Carminati et al., 1998; Wortel and Spakman, 2000; 2004; Rosenbaum et al., 2008; van Hinsbergen et al.,

2010; Chertova et al., 2014; Spakman et al., 2018), the Anatolia-Zagros orogen (Şengör et al., 2003; Faccenna et al., 2006), and Himalaya and Tibet (van Hinsbergen et al., 2012; Wu et al., 2014; Liang et al., 2016). These studies often ascribe short-lived, long-wavelength exhumation events or sudden pulses in sediment supply to slab breakoff. However, they often neglect the influence of the 3D geometrical configuration of each tectonic regions. How likely was the tectonic setting in those domains to have caused the slab tearing in the first place? How much does slab breakoff contribute to the buoyancy-driven isostatic surface uplift? Our study addresses these phenomena, taking the Gibraltar Arc in the westernmost Mediterranean as a reference geological region.

Despite being severely debated, most authors agree that the tectonic reconstructions of the Western Mediterranean involve subduction rollback (35 Ma) as the key geodynamic process that drives the tectonic evolution. The disagreements among the proposed models lie in how this rollback couples with tectonic evolution. The main three proposed rollback scenarios (summarized in Chertova et al., 2014) are: (i) rollback originates from a laterally restricted NW dipping slab confined to the Baleares (Rosenbaum et al., 2002; Spakman and Wortel, 2004; de Lamotte et al., 2009; Van Hinsbergen et al., 2014) ; (ii) rollback originates from a long N-NW dipping subduction zone stretching from the Baleares in the north-east to Gibraltar in the west margin (Faccenna et al., 2004; Jolivet et al., 2009); or (iii) rollback originates from a SE dipping subduction under the north-African margin (Vergés and Fernàndez, 2012). The major extension of the Alboran domain ended during the middle Miocene (~16 Ma) (e.g. Vergés and Fernàndez, 2012).

Based on seismic tomographic imaging, Spakman and Wortel (2004) suggested that slab tearing might have occurred in the Gibraltar Arc region as a consequence of the continental convergence and the subsequent slab rollback declined during early Miocene. The biostratigraphic studies by Krijgsman et al. (2018) and van der Schee et al. (2018) revised the age of the uplift and provided a new age constraint on the western Betic intramountain basins to be older than 7.51 Ma (late Tortonian). The vertical movements (uplift) observed in the Internal Betic zone after late Tortonian are best constrained from the present elevation of tectonically undeformed Miocene marine sediment in that region (marine to non-marine transition), often above 600 m elevation (Garcés et al., 1998; Iribarren et al., 2009). This has been interpreted as the result of a westward migration of a lateral tear within the steeply hanging Ligurian-Tethys slab seen in tomography (Garcia-Castellanos and Villaseñor, 2011). Slab tearing occurred in previous thermomechanical models by Chertova et al. (2014) and Spakman et al. (2018), with the objective of optimizing the fit between observed and predicted present slab morphology. However, the timing of this mechanism has been poorly constrained and prompting questions regarding the timing, the duration and the topographic response of the tearing process.

The uplift of the intramountain basins within the Betics and Rif (Fig 1), possibly caused by the slab tearing, has been linked to the closure of the marine gate-

way across the Gibraltar Arc during the Late Miocene which led to the partial desiccation of the Mediterranean Sea, (Messinian Salinity Crisis; MSC) (Garcia-Castellanos and Villaseñor, 2011; Coulson et al., 2019). According to this hypothesis, once the marine gateways closed off due to the regional epeirogenic uplift, it triggered the massive salt accumulation of the MSC (5.96–5.33 Ma), possibly the most abrupt environmental change on Earth since the beginning of the Tertiary.

This study aims to understand the lithospheric slab tearing process and the consequent surface uplift, through 3D thermomechanical modelling. The initial model setup in this study is based on the tectonic setting from the reconstruction of the Western Mediterranean, where a S-SE slab rolls back and collides with an oblique margin (e.g. Vergés and Fernàndez (2012)). However, we just intend to study the tearing process, we do not plan to model the previous evolution of the slab. We will investigate how different scenarios and/or parameters act on the initiation of the slab tearing and its propagation along the trench, and quantify the resulting surface elevation changes robustly coupled with the deep geodynamic processes (viscous flow, temperature evolution, and dynamic topography). In addition, we will provide insights into how the slab tearing dynamics fit within the realm of the Western Mediterranean, and how these surface vertical motions help constraining the Messinian Salinity Crisis event.

1.

Method

(a)

Model setup

The continental convergence is modelled with an incoming continental block, overriding a subducting oceanic plate, which is connected to a stationary continental block through a passive margin. The model region is based on the tectonic reconstruction by Vergés and Fernàndez (2012) and also compatible with the model proposed by Spakman and Wortel (2004) and van Hinsbergen et al. (2014), where a subduction zone progresses towards an oblique continental passive margin ('model' box in Fig 1). The 3D model domain (Fig 2) measures 1500 km × 780 km × 1200 km, with the resolution of 4.6 km× 3.0 km × 4.6 km, in the x, y (vertical), and z directions, respectively. The 40-km thick continental crust splits into the upper (20 km) and lower (20 km) continental crust, and thinning toward the ocean. The 8-km thick oceanic crust also splits into the upper (basaltic, 3 km) and lower (gabbroic, 5 km) oceanic crust. Partial melting and melt extraction processes are neglected in order to keep our models simplified and the interaction between the slab tearing and the crust isolated.

The viscous flow law of 'wet quartzite' describes the behaviour of both the upper continental crust and the upper oceanic crust, while the 'Plagioclase

An75' describes the behaviour of the lower continental crust and lower oceanic crust (Table 1, Ranalli, 1995). The lithospheric mantle, asthenospheric mantle, and mantle 'weak zone' (less viscous mantle material) all have a 'dry olivine' rheology (Table 1, Hirth and Kohlstedt, 2003). The weak zone is prescribed in front of the incoming continental plate (Fig 2a, c) to assist with the subduction initiation. Two weak zones are also prescribed on both the eastern and western side of the incoming continental plate as a way to decouple the moving plate from the surrounding oceanic domain (Fig 2a, c).

In the first stage of the experiment, the prescribed convergence velocity is pushing from a plane at x=1389 km, and at the depth of y=21–147 km (upper lithospheric mantle). This plane is labelled 'ridge' in Fig 2c. The first stage of the experiment involves a forced convergence until the slab reach 200 km depth. After the first stage, the obtained thermo-mechanical state is then used as an initial setup for continental convergence. In the second stage, the prescribed convergence rate is either removed, so that the slab sinks due to its own weight (Mod1-reference, Mod2, Mod3, and Mod4), or reduced to a lower value of 4 mm/yr (still pushing from the 'ridge' at x=1389 km), resembling the convergence rate in the Western Mediterranean (Mod5) (Macchiavelli et al., 2017).

Boundary conditions

The velocity boundary conditions are free slip for the left (x=0 km), right (x= 1500 km), front (z=0 km), back (z=1200 km), and top boundaries (y=0 km). The bottom boundary (y=780 km) is open/permeable, allowing rock materials to flow in or out of the model domain. For the bottom boundary, an external outflux boundary implies zero shear stress conditions and constant normal velocity to be satisfied at ~300 km below the base of the model domain, which ensures the mass conservation within the computational domain (e.g. Burg and Gerya, 2005; Gerya et al., 2008; Li et al., 2013).

The elevation of the lithosphere is calculated dynamically as an internal free surface through a buffer layer of 'sticky air' ($_{air} = 10^{18}$ Pa $\cdot$ s, $_{air} = 1$ kg/m^3) (Gerya and Yuen, 2003; Schmeling et al., 2008; Crameri et al., 2012). It is 22 km thick on top of the continental plate and 25 km on top of the oceanic plate. We implemented a simplified erosion condition in our model, where instantaneous sedimentation limits a trench depth to 8 km below the water level and the instantaneous erosion is prescribed at 8 km above the initial continental crustal surface where rock markers change into sticky-air markers.

The continental geotherm is prescribed as a linear variation from 0°C at the model surface (y 22 km, air) to 1344°C the lithosphere-asthenosphere boundary (y=110 km) (Jiménez-Munt et al., 2019; Kumar et al., 2021). The initial thermal structure of the oceanic lithosphere is calculated using the half-space cooling model (e.g. Turcotte and Schubert, 2014) based on a slab age of 110 Ma. The initial adiabatic temperature gradient of 0.5°C/km is prescribed in the asthenospheric mantle (Katsura et al., 2010). For the initial thermal boundary

conditions, the upper boundary has a fixed value of 0°C, and zero horizontal heat flux across the vertical boundaries. Similar to the velocity boundary, the bottom thermal boundary is permeable such that the temperature and vertical heat fluxes can vary along the lower boundary. This implies that the constant temperature condition is satisfied at ~300 km below the bottom of the model box (e.g. Burg and Gerya, 2005; Gerya et al., 2008; Li et al., 2013).

Governing equations

The modelling in this work was carried out using a 3D thermo-mechanical coupled numerical code, 'I3ELVIS' (Gerya, 2013). The code is based on finite-differences and marker-in-cell numerical schemes (Gerya and Yuen, 2003; Harlow and Welch, 1965). The governing physical laws such as conservation of mass, conservation of momentum, and heat equation are discretised on a staggered Eulerian grid. For each time step, fourth order Runge-Kutta scheme spatially advects the markers. The multi-grid method is used to speed up the convergence of the Gauss-Seidel iterative solver.

(1) The conservation of mass is described by the continuity equation of an incompressible viscous medium:

$$\frac{\partial v_i}{\partial x_i} = 0, \quad (1)$$

where v is the flow velocity and where i (as well as j shown hereafter) is index, which denotes spatial directions i, j = (x,y, z) in 3D using Einstein notation.

(2) The conservation of momentum is described by the Stokes equation for creeping flow, which states:

$$\frac{\partial \sigma'_{ij}}{\partial x_j} - \frac{\partial P}{\partial x_i} = -\rho(T, P, c) g_i, \quad (2)$$

where σ'_{ij} is the deviatoric stress tensor, P denotes the total pressure (Pa), and g is the gravitational acceleration (m/s^2). In this form, we consider the Boussinesq approximation, where the density $\rho(T, P, c)$ in the buoyancy term ρg_i varies locally as a function of temperature (T), pressure (P), and composition (c).

$$\rho C_p \frac{\mathrm{DT}}{\mathrm{Dt}} = \frac{\partial}{\partial x_i}\left(k \frac{\partial T}{\partial x_i}\right) + H_r + H_a + H_L + H_s, \quad (3)$$

(3) The heat balance in a convective medium is described by the heat conservation equation, which states:

where C_p is the heat capacity (J/K), T is temperature (K), k denotes thermal

conductivity (W/(m · K), which is a function of temperature, pressure, and composition, i.e. k(T, P, c) , H_r is radioactive heat production, H_a is adiabatic heat production/consumption, H_L is latent heat production/consumption (due to phase transformation), and H_s is the shear heat production (a product of deviatoric stress and strain rate), more details in Gerya and Yuen (2003, 2007).

1. **Density model and phase changes**

The rocks' densities vary with temperature T (K) and pressure P (Pa) according to the equation of state:

$$\rho_{P,T} = \rho_0 \left[1 - \alpha(T - T_0) + \beta\,(P - P_0)\right], \quad (4)$$

where ρ_0 is the reference density at $P_0 = 1$ MPa and $T_0 = 298.15$ K, the coefficient of thermal expansion $\alpha = 2{\times}10^{-5}$ 1/K, and the coefficient of thermal compressibility $= 6{\times}10^{-12}$ 1/Pa. Our models take phase transition of olivine in the mantle into account. As the dry olivine is subjected to greater pressure at depths, it first undergoes exothermic phase transition (~ 410 km) and transforms into wadsleyite (Katsura and Ito, 1989). At a greater depth and pressure, the wadsleyite exothermically transforms into ringwoodite (~ 520 km), which decompose (endothermically) into bridgmanite (silicate perovskite) at an even greater depth (~ 660 km) (Ito et al., 1990). The eclogitization of the subducted oceanic crust (basaltic and gabbroic) is taken into account by linearly increasing the density of the crust with pressure from 0% to 16% in the P-T region between the experimentally determined garnet-in and plagioclase-out phase transitions in basalt (Ito and Kennedy, 1971).

1. **Visco-plastic rheology**

The composite visco-plastic (VP) rheology is used with no elasticity because the model aims to study slab tearing process in a more simplified system. The elasticity might affect the lithospheric flexure and uplift, however, the visco-plastic rheology is suffice to establish the general dynamics of continental convergence and the underlying mantle flow (Gerya and Yuen, 2003, 2007). The ductile rheology (η_{ductile}) is approximated by a combination of effective viscosities for diffusion η_{diff} and dislocation η_{disl} creep. We assume that the total strain rate is the sum of the strain rates due to diffusion creep and dislocation creep, and that they act in parallel and independently from each other.

$$\eta_{\text{ductile}} = \frac{1}{\frac{1}{\eta_{\text{diff}}} + \frac{1}{\eta_{\text{disl}}}} \quad (5)$$

(1) In the crust, we assume constant grain size and η_{diff} and η_{disl} is computed as:

$$\eta_{\text{diff}} = \frac{A}{2\sigma_{\text{cr}}^{(n-1)}} \exp\left(\frac{E+PV}{\text{RT}}\right) \quad (6)$$

$$\eta_{\text{disl}} = \frac{A^{\frac{1}{n}}}{2} \exp\left(\frac{E+PV}{\text{nRT}}\right) \dot{\varepsilon}_{\text{II}}^{\frac{(1-n)}{n}} \quad (7)$$

where R is gas constant (8.314 J/(K $\cdot$ mol)), P is pressure (Pa), T is temperature (K), $\dot{\varepsilon}_{\text{II}} = \sqrt{1/2(\dot{\varepsilon}_{\text{ij}})^2}$ is the the second invariant deviatoric strain-rate tensor, $_{cr}$ is the critical stess, A is the pre-exponential factor (Pa$^{\text{n}}$ $\cdot$ s), E denotes activation energy (J/mol), V is activation volume (J/Pa), and n is the stress exponent of the viscous creep (Table 1).

(2) In the mantle, the ductile creep is implemented with grain size growth and reduction processes. In the case of the mantle, the composite rheology in Eq. 5 still stands,

$$\eta_{\text{diff}} = \frac{1}{2} A_{\text{diff}} \, \text{h}^m \exp\left(\frac{E_{\text{diff}}+PV_{\text{diff}}}{\text{RT}}\right) \quad (8)$$

$$\eta_{\text{disl}} = \frac{1}{2} A_{\text{disl}}^{\frac{1}{n}} \exp\left(\frac{E_{\text{disl}}+PV_{\text{disl}}}{\text{nRT}}\right) \dot{\varepsilon}_{\text{II}}^{\frac{(1-n)}{n}} \quad (9)$$

where, A_{diff} is the experimentally determined pre-exponential factor for diffusion creep (Pa $\cdot$ s) and A_{disl} is pre-exponential factor for dislocation creep (Pa$^{\text{n}}$ $\cdot$ s), h is grain size (m), m is the grain size exponent (Table 1).

The viscous rheology is combined with a brittle rheology to compute an effective visco-plastic rheology, based on a Drucker-Prager yielding criterion (e.g. Ranalli, 1995):

$$\eta_{\text{ductile}} \leq \frac{C+\mu P}{2\dot{\varepsilon}_{\text{II}}} \quad (10)$$

_1 , &> _0 (11)

$$\gamma = \int \sqrt{\frac{1}{2}\dot{\varepsilon}_{\text{ij(plastic)}}^2}\text{dt} \quad (12)$$

where μ is the internal friction coefficient (μ_0 and μ_1 are the initial and final internal friction coefficient, respectively), $\mu_\gamma = (\mu_0 - \mu_1)/\gamma_0$ is the rate of faults weakening with integrated plastic strain γ (γ_0 is the upper strain limit for the fracture-related weakening), C is the rock compressive strength at $P = 0$, t is time (s), $\dot{\varepsilon}_{ij(\text{plastic})}$ is the plastic strain rate tensor (Table 1).

Results

All of the experiments incorporate two stages. The first stage consists of forced convergence until the slab reaches 200 km depth. The second stage uses the output from the first stage as an initial setup and continues on as the slab undergoes either free-subduction (Mod1-reference, Mod2, Mod3, and Mod4) or fixed convergence velocity (Mod5). The numerical experiments were performed using 24 cores on the ETH-Zürich EULER cluster. Note that all model time 't' (in Myr) are given from the initiation of stage 2 for each model.

Reference model (Mod1-reference)

After the slab has reached the depth of 200 km, the prescribed convergence rate stopped. As the dense slab continues to sink under its own weight (Table 1), the Iberian continental margin started to bend downward and the incoming block overrides the passive margin. At t=3.84–4.10 Myr, the lithospheric thinning/necking started on the slab's easternmost side (z=800 km) at 120 km depth (Fig 3c). Immediately after the detachment, at 4.24 Myr, the incoming continental block came to a complete stop, which, in turn, causes a change in the slab's downward velocity. The slab's portion in the vicinity of the tearing appear to have lowered downward velocity, which means the attached portion of the slab continues to sink with a faster downward velocity (Fig 3c, d). The tearing point propagates westward reflecting in the tilted angle of the slab's top edge as shown in the Fig 3e and Fig 4.

While the slab is fully attached, the down-dip motion of the slab induced corner flows, and the large slab body induced a large flow around the slab's edges (Fig 5). The initiation of slab necking and tearing on the eastern side is inherent to our model setup because the slab's easternmost part is the only region in which the continental-continental convergence occurs (Fig 4a1). Once the tearing caused the incoming block to stop completely, the tear propagates westward. As you look westward, the subsequent tearing now is a result of the tearing process that has been set in motion from the east, and not a tearing due to continental-continental convergence. The different amount of exhumed oceanic crust in the forearc wedge (Fig 4b2, c3) appear to be depending on how large the remaining oceanic domain is in between the incoming African plate and the Iberian plate. We observe a larger amount of exhumed oceanic crust in the westernmost side (Fig 4c3).

This initiation of slab tearing is observable as a sharp surface uplift along the collisional belt, with uplift rate ranges from 0.23 mm/yr to 2.16 mm/yr throughout the tear propagation. The rise in elevation (Fig 4a, b, c) also evolves westward, reflecting the tear propagation occurring deeper in the mantle. The tearing occurs due to great stress in the bending zone created by both the buoyancy of the Iberia block (upward force) and the weight of the hanging slab (downward force). The slab is completely detached after t=5.75 Myr (tearing duration of ~1.65 Myr).

1.

Influence of model parameters

(a)

Effect of no incoming continental block (Mod2)

The reference model (Mod1-reference) had an incoming buoyant continental block implemented to create a continental-continental collision, which then led to a one-sided slab tearing. We now move on to look at how the lack of this incoming buoyant continental block would affect the subduction zone dynamic. Rheologically, Mod2 mimics Mod1-reference but the absence of an incoming continental block creates a continental-oceanic arc. At t=3.48 Myr, the retreating intra-oceanic subduction trench reaches the continental passive margin, after which the trench continues to retreat. After 0.5 Myr, high topography developed over the trench (Supplementary Fig S1a). Here on the eastern side of the slab, the accumulation of crustal materials above the trench prevented the trench from retreating any further and led to the initiation of slab tearing at t=4.66 Myr. The slab is completely detached by t=5.70 Myr (tearing duration of ~1.04 Myr). The uplift rate during the tear propagation ranges from 0.71 mm/yr to 1.35 mm/yr. The lack of incoming continental block thus does not prevent the initiation of slab tearing.

In Mod2, where the overriding plate does not have a buoyant continental block, the slab-tearing dynamics are similar to the Mod1-reference, likely since both models have the same mantle rheological setup. Mod2's lack of a buoyant continental block on the overriding plate does not appear to hinder the rate of trench retreat that is thus mainly controlled by the oceanic slab buoyancy and asthenospheric mantle viscosity. In Mod1-reference, the presence of an incoming buoyant continental block does limit the extent of the forearc region, as illustrated in Fig 6. A less dense body (relative to the surrounding mantle) rises up the subduction channel and thrusts under the overlying crustal materials (Fig 6c, e, and f). The lighter mantle pushed-up crustal material then spread over the forearc region at the surface. The absence of a continental block in Mod2 allows the crustal material to spread farther compared to Mod1-reference, where the spreading is limited by the buoyant continental block.

Effect of a higher ductile viscosity of the mantle (Mod3)

The subduction in the reference model is spontaneous i.e. the slab falls by its own weight resulting in the subsequent trench retreat. However, the slab sinks with a velocity far greater than what we would expect in the Western Mediterranean region. Another model was constructed with a more viscous mantle, which can be achieved by increasing the ductile viscosity through increasing the activation volume of the mantle (both V_{diff} and V_{disl}), in the hope of slowing down the down-going slab due to the increased resistance of the higher-viscosity sublithospheric mantle. In the model Mod1-reference, the activation volume

for the dislocation creep was V_{disl}=2.6 J/(mol · MPa) and for diffusion creep V_{diff}=0.7 J/(mol · MPa), and in this model Mod3, V_{disl}=3.0 J/(mol · MPa) and V_{diff}=0.8 J/(mol · MPa) (Table 1). The increased activation volume means the stronger mantle viscosity increase with pressure (and therefore with depth). The evolution of the subduction is similar to the reference model but with much slower rate. For example, when the slab has reached 450 km depth, the slab in Mod1-reference has a maximum downward velocity of 20 cm/yr (t=3.05 Myr) where as Mod3's maximum downward velocity is 8 cm/yr (t=6.87 Myr). The slab tearing in Mod3 initiated at around t=11.08 Myr as oppose to t=4.34 Myr in the reference model. The surface topography above the initiation of tearing exhibits an elevation of ~1.5 km (Supplementary Fig S2d), which is similar to Mod1-reference. The uplift rate during the tear propagation ranges from 0.75 mm/yr to 1.68 mm/yr. In Mod3, the slab tear initiated at t=9.80 Myr and the slab completely detached by t=12.95 Myr (tearing duration of ~1.87 Myr).

The less viscous mantle in the reference model allows the slab to sink down with ease, which resulted in the trench retreat at the rate of 20 cm/yr. The more viscous mantle in Mod3 offers higher resistance for the down-going slab and results in the trench retreat rate of 10 cm/yr. The upper few 100s km of Mod3's upper mantle still has a low viscous mantle (Supplementary Fig S2), meaning that the slab's strong negative buoyancy is still not well supported at those depths. This explains the still large rollback and slab tearing speeds that are obtained.

The fast down-going slab, together with the fast trench retreat velocity in the reference model, causes segments of high stress (4–5 MPa) and high strain-rate (10^{-14}–10^{-12} 1/s) to develop at the depth of greater than 120 km which led to a deeper breakoff depth. In Mod3, with more viscous mantle, the down-going slab is better supported by the surrounding asthenosphere leading to a more gradual and shallow stress build-up focussing within the bending zone of the slab. This shallow stress focussing, at the depth of less than 100 km, led to a shallower breakoff compared to the reference model.

Effect of an increased brittle strength of the mantle (Mod4)

Another way to increase the viscosity of the mantle is to increase the brittle viscosity, i.e. the upper limit of the visco-plastic viscosity. Similar to Mod3, the increased mantle viscosity in Mod4 aims to slow down the sinking slab such that we can study the characteristics of slab tearing, which evolved too quickly between modelling time-steps in Mod1-reference. In Mod4 model, we increased final internal friction coefficient ($_1$ in Eq. 8) for the lower oceanic crust and the mantle, from zero in Mod1-reference to 0.3 in Mod4 (Table 1). By increasing this coefficient value: (1) we decrease the rate of strain weakening by a factor of two; and (2) we significantly increase the effective visco-plastic viscosity of deformed cold lithospheric mantle at elevated pressures/depths. After the initial push, the slab failed

to sink down into the asthenosphere on its own due to a high resistance to local brittle/plastic deformation associated with the slab retreat and bending. This lack of slab's downward velocity also led to the termination of trench retreat altogether (Supplementary Fig S3). The slab only reached 300 km in depth and hang there with the angle of the hanging slab slightly steepened. The lack of trench retreat means the incoming continental block did not reach the passive margin and so there is no collision and no slab tearing. This rheological setup with strong brittle/plastic- mantle, therefore, does not favour the slab tearing.

Effect of fixed the convergence velocity (Mod5)

In model Mod5, we took the first stage of the reference model (initial push, slab reaches the depth (y) of 200 km) and enters the model into the second stage with an imposed relative convergence. The imposed plate convergence velocity is set to 4 mm/yr to mimic the average convergent velocity between the Iberian and African plates (Macchiavelli et al., 2017). This velocity is much slower than the velocity resulting from the hanging slab in previous runs, so this change should slow down the slab retreat. Such slow velocity exposes the hanging slab to a fast thermal diffusion in the surrounding asthenosphere. No slab tearing occurs in this model, but instead a lithospheric dripping takes place (Supplementary Fig S4).

The low convergent velocity of 4 mm/yr causes the slab to experience a greater degree of thermal diffusion than thermal advection and, therefore, could not maintain its low internal temperature and high density, all of which led to thermal erosion and lithospheric dripping (Supplementary Fig S4). The great amount of thermal diffusion that the slab experienced and the amount of time that the slab is hanging in the sublithospheric mantle allow an arcuate (in plan-view) deformed lower-viscosity slab to develop. In the models with spontaneous subduction (Mod1-reference, Mod2, Mod3, and Mod4), the subduction and trench migration comes to a stop once the slab reached the passive margin and the tear has started. In Mod5, however, the continuous pushing of the incoming continental block creates a band of high elevation over the arcuate trench (Supplementary Fig S4d).

1.

Discussion

(a)

Geometry of the passive margin and slab-tearing dynamics.

The lateral slab tearing has been invoke to explain some observations, such as the seismicity pattern in the Vrancea slab (Mitrofan et al., 2016) or the seismic tomography in the South Iberian margin, Apennines and Hellenic arc (Wortel, 2000). Previous 3D numerical models of subduction that exhibited slab tearing, such as those by van Hunen and Allen (2011); Duretz et al. (2014); Magni et al. (2017), all utilised a straight passive margin, which ended up producing slab tearing in the slab interior rather than on the slab edge. However, in this work, the models included an oblique continental passive margin, which added asymmetry to the collision process. Balázs et al. (2021) by 3D thermo-mechanical subduction models, already found that an oblique oceanic subduction results in strain partitioning in the accretionary wedge which can contribute to different subduction velocities.

The results from our Betics-inspired models suggest that the obliquity of the continental passive margin has great influence over the initiation of slab tearing because it promotes a laterally diachronous continental collision, which leads to slab tearing. In our models, the oblique passive margin gave rise to an east-to-west slab tearing. Averaging over approximately 500 km distance, the tear velocities are 42.6 cm/yr in Mod1-reference, 67.6 cm/yr in Mod2, and 37.6 cm/yr in Mod3 (Table 2). Our tear propagation rates fall well within the range of previous estimations: 7−45 cm/yr from the Carpathians' depocenter migration by Meulenkamp et al. (1996) from the evolution of the Carpathian-Pannonian system whose geological model was constructed using regional chronostratigraphic sequences; and 10−80 cm/yr from 3D numerical modelling of continental collision by van Hunen and Allen (2011). A 3D stress model, as a function of rheology, tears length, and force distribution, by Yoshioka and Wortel (1995) showed a tear propagation rate in the range as wide as 2−94 cm/yr.

Overall, the slab takes less than 2 Myr to completely detach (over the entire slab length of 600–700 km), which is fast on a geological timescale (compared to the timescales needed for subduction). The factor that seems to have some control over the timing of the tearing is the mantle rheology. The viscosity of the sublithospheric mantle in Mod3 is 10^{22} Pa $\cdot$ s whereas it is 10^{21} Pa $\cdot$ s in Mod1-reference. The more viscous sublithospheric mantle in Mod3 slowed down the sinking slab, hence the slowest tear-propagating velocity. Chertova et al. (2014) and Spakman et al. (2018) used numerical models to optimize the fit between a slab morphology, as predicted by a geodynamic model, and the seismic tomographic models. The lower mantle in their numerical models has a viscosity of 2×10^{22} Pa $\cdot$ s which is higher than the value used in our models, hence their slow rollback speed and slow east-to-west slab tearing under the Betics. The sublithospheric mantle viscosity in our models allows the slab to sink faster and, therefore, leads to faster tearing velocity. Chertova et al. (2014) illustrated that in order to create an arcuate slab, such as that imaged under the Western Mediterranean; a variable rollback speed along the strike of the

trench is needed. However, the slab rollback in our models was terminated early (where the slab is still attached) due to being exceeded by the fast lateral tearing velocity, hence, the lack of an arcuate slab in our models. This early termination of the slab rollback is also why the gap between the trench and the passive margin exist (Fig 6a-c). A slower slab tearing would allow the slab rollback to continue in the region where the slab is still attached, and the western trench could reach the passive margin (Spakman et al., 2018) forming an arcuate shape. Using a geodynamic model, Peral (2020) explains the curvature of the slab by pinning the western edge to the west-Africa continental block, while the NE slab retreats free along the transform fault. Schliffke et al. (2021) also found by numerical modelling that the continental collision with an irregular passive margin, can form highly arcuate orogenic belts, but also as a result of the associated transient stress changes it can cause complex geological processes in the overriding plate, processes observed in the Gibraltar arc.

The ranges of breakoff depth from our models are 80−150 km on the eastern side and 170−200 km on the western side. These ranges fall within similar ranges as previous numerical modelling studies such as 80–240 km from Freeburn et al. (2017), 95–140 km from Schellart (2017), 100–400 km from Gerya et al. (2004), and 120–145 km from Duretz et al. (2014). The difference in breakoff depths could plausibly come from the different rheological setting in each numerical model, as well as different tectonic setup. In the models presented here, the slab's eastern side has a shallow tearing depth, which could be caused by the weakness in the transition zone between the continental and the oceanic lithosphere. While on the western side the tearing depth is deeper as the tear, here, is not only caused by the tectonic variation of the transition zone but also: (i) the negative buoyancy of the hanging and detached portion of the slab; and (ii) the high velocity mantle influx in the slab tear window (Fig 5). A similar pattern is reflected in the breakoff location. On the easternmost side, the breakoff tends to occur within the subducted continental lithosphere portion, such that the detached slab pinched out some continental crust. Since the slab tear depth is deeper westward, therefore, the breakoff tends to be within the subducted oceanic lithosphere portion.

1.

Surface uplift

(a)

Dynamic topography

There are two components which are thought to be shaping the surface topography we observed today, the crustal isostatic compensation effect and dynamic topography (Forte et al., 1993). Dynamic topography is caused by the buoyancy-driven mantle convection exerting vertical stress onto the lithosphere. Dynamic subsidence is caused by downward mantle flow (downwelling), while dynamic

uplift is caused by upward mantle flow (upwelling).

Fig 7 shows model Mod3's modelled density distribution and the evolution of the
modelled elevation, and the two contributions, the isostatic and the dynamic components. We calculated the isostatic effect with a compensation depth of 150 km (128 km below crustal surface). This isostatic elevation is due to the density changes at crustal and lithosphere scales, without accounting the dynamics of the slab subduction.

The dynamic topography then came from taking the isostatic effect away from the modelled elevation. The dynamic topography shown in Fig 7 appears to be reflecting properly the mantle dynamics. From the dynamic topography results, we can identify the slab pull effect
with a subsidence and the corner flow and mantle upwelling with an uplift. Prior to slab tearing, the mantle flowing upwards in the subduction channel corresponds with the high dynamic topography (Fig 7a, b). After tearing has begun, the tearing gap allows the mantle flow to go through and this channel upward flow is reduced (Fig 7c, d and Fig 5). While the slab is still intact, the slab-pull force is transmitted up to the crustal surface, producing the subsidence on the passive margin (Fig 7a, x=250-300 km). As the slab starts necking and tearing, this transmission of slab-pull force reduces and, therefore, reducing the aforementioned subsidence (Fig 7c, d). The mantle convection cells re-established themselves when the detached slab is a depth of 450–660 km (Fig 7d).

We also set out to look at the time-response of surface topography to tearing in the mantle and the possible temporal delay involved. The one-to-one (instantaneous) interpretation has been widely utilised by previous studies (Lithgow-Bertelloni and Silver, 1998; Boschi et al., 2010; Faccenna and Becker, 2010; Faccenna et al. 2014; Gvirtzman et al., 2016; Heller and Liu, 2016; Austermann and Forte, 2019; Ávila and Dávila, 2020). However, our methodology could not resolve such significant temporal lag between the deep process of tearing and the
surface topographic response. The tearing in our models occurs at a relatively fast velocity,
which may make it difficult to capture and quantify this delay.

Uplift signature

Fig 8 displays the modelled evolution of the topographic response as the slab tearing laterally propagates westward. The incoming continental block collided with the passive margin and subsequently came to a complete stop. The initial continental-continental collision (prior to tearing) caused a high topography (1 km high) on the eastern side (z=800 km) (Fig 8a and e). As the tear propagates westward, the elevation increases in the same direction (Fig 8b, c, d). The increase in surface elevation does not occur only above the tear position but also in the proximate area, as shown in Fig 8e and 8f that the highest amount of

uplift is not necessarily in the same location as the tear. A possible explanation is that as a tear gap opens, it permits a higher density of poloidal flow to flow through, which induces trenchward mantle flow. This rush of poloidal flow then induces a basal drag that drives trenchward motions under the two colliding plates. This trenchward motion exerts compressional force to the relatively immobile subduction zone hinge, in addition to the opposing force from the collision, leading to an uplift of 0.3–0.8 km even before the arrival of the tear (Fig 8e). Jiménez-Munt et al. (2019) estimated similar values of the pulled down topography by the Strait of Gibraltar slab. As the tearing propagates further westward, the high topography on the eastern side starts to subside by as much as 0.2 km (Fig 8e).

As the slab sinks further, its volume in the mantle increases, obstructing the mantle flow and giving rise to corner flow in the mantle wedge. The corner flow increased the velocity of mantle convection (by 3–10 cm/yr, Fig 7a), which gave viscous support to the overlaying crusts. As slab tearing initiates, it immediately opens up a new channel, which the mantle quickly flows through to replace the volume previously taken up by the slab. This sudden rush of mantle flow could be giving viscous support to the overlying crust (Fig 7a, b, c), which leads to the sudden surface uplift (modelled elevation and isostatic compensation), a prominent signature of slab detachment. The dynamic topography, corresponding to the aforementioned mantle-flow rush, decreases (Fig 7a, b, c) as slab tearing has started on the eastern side (z = 800 km) and thus the exhumation and corner flow is reduced in velocity.

The mantle convection around the detached and sinking slab remains strong at this stage as the slab sinks at such a steep angle that it still obstructs mantle flow (Fig 7c). After the detached slab sinks further down, the bottom of the slab hits the depth of 660–700 km discontinuity and rest there, which causes the slab to begin to sink in a flatter manner (e.g. Fig 3f). As the detach slab lays flatter, the mantle convection velocity reduces (by 3–10 cm/yr), or return to normality (4 cm/yr), because now there is no large body to obstruct the mantle flow and neither a heavy slab pulling down the mantle. This reduced velocity of mantle convection means there is less mantle dynamics going on, which would reduce the dynamic support that was exerting onto the crust. The crust and the lithospheric mantle begin to readjust, thermally, and the previously uplifted surface (by 0.5–1.0 km) begins to subside. Overall, the surface uplift rates observed in our models, as a response to the slab tearing, range from 0.23–2.16 mm/yr. The predicted surface uplift rates previously quantified by numerical modelling studies range widely as low as 0.10 mm/yr to as high as 2.65 mm/yr (Andrews and Billen, 2009; Duretz et al, 2011).

Supplementary Fig S5 shows the stacked time-evolution of surface elevation of the slice from Mod3 at position z=780 km. As the subduction zone was approaching the passive margin, the continental block on the overriding plate exhibit an elevation of ~0.8 km (Supplementary Fig S5a). Once the trench has contacted with the passive margin (at ~9 Myr) and the tearing process has

initiated, the accretionary wedge gave rise to a surface elevation of up to 2 km in the forearc area southwards of the trench line (Supplementary Fig S5b). High elevation areas (~2 km) on the continental passive margin also increase as the subduction zone pushed northwards. After a period of slab detachment, 1.9 Myr for Mod3, both the continental block on the overriding plate and the accretionary wedge decrease in topography (after 11.70 Myr, Supplementary Fig S5). The area on the passive margin, northern of the compression zone (x=150–180 km), also start to subside with elevation decreased as much as 0.5 km. This subsidence of the passive margin could be because of the lithospheric cooling due to the absence of heat flow from the lower mantle. This artefact could also be observed in the decrease in elevation in Fig 8e and Fig 8f on the westernmost side.

Implications for the Western Mediterranean

The oblique nature of the southern Iberian margin may have played a key role in triggering slab tearing from one end of the slab, similar to our models. Based on a tectonic reconstruction of the Ligurian-Tethys between Iberia and Africa during the Late Cretaceous, Vergés and Fernàndez (2012) proposed that a SE-dipping subducted slab started retreating under the NW African margin and retreated NW-wards to the present-day Gibraltar Arc location (Fig 1). The subduction would imply an initial oblique collision at the margin between Iberia and Africa. Alternatively, looking at the tectonic reconstruction of the same region as proposed by Rosenbaum et al. (2002a), Spakman and Wortel (2004), and Van Hinsbergen et al. (2014), where the initially short subduction started from the Baleares, elongated, split up, and then rotated westward into the Gibraltar Arc System. The portion of the subduction zone that moves into the Gibraltar Arc System would also be on a collision course with the oblique southern Iberian margin. Therefore, both tectonic reconstructions could potentially lead to the slab tearing from one side as observed in the interpreted seismic tomography of the Western Mediterranean (Spakman and Wortel, 2004).

Chertova et al. (2014) used 3D numerical modelling to model 3 evolution scenarios of the Western Mediterranean, with the goal of optimizing the fit between the slab morphology after 35 Myr (as predicted by a geodynamic model) and the observed seismic tomography. Spakman et al. (2018) and Capella et al. (2020) used 3D numerical modelling, together with geological and geodetic data, to propose that the enigmatic tectonic features in the Western Mediterranean (e.g. the closure of marine gateway prior the Messinian Salinity Crisis, the shortening of the Rif, and the eastern Betics extension) could be the effect of slab dragging. Negredo et al. (2020), through thermo-mechanical modelling of continental-edge delamination across STEP faults following slab-tearing, suggested that the stability of the evolution regime in the central Betics is sensitive to the initial rheological and thermal conditions. Our models differ from previous works of the region because they are not trying to model the evolution of the region. Instead, the Western Mediterranean was used as an inspiration to model the

relationship between slab tearing and surface uplift because such interaction has previously been proposed in this region (Garcia-Castellanos and Villaseñor, 2011; Spakman et al. 2018). Our model brings the surface-uplift component into play, which connects the mantle dynamic with the surface uplift. The uplift rates from this work (0.23 mm/yr to 2.16 mm/yr) are consistent with the situation during the first stage of the MSC event, in which the uplift of the seaway is compensated for the erosion of seaway, allowing continuous but limited water inflow from the Atlantic into the Mediterranean Sea. The tectonic and erosion model by Garcia-Castellanos and Villaseñor (2011) proposed that a critical uplift rate of 5 mm/yr is needed to close the seaways across the Gibraltar Arc. Coulson et al. (2019) built upon Garcia-Castellanos and Villaseñor (2011)'s model by incorporating an ice-age sea level theory, which predicts a critical uplift rate of < 1.5 mm/yr.

Previous biostratigraphic studies in the Betics suggested that the age of marine uplift in the region was in the range of 10–8 Ma, younging westward (Garcés et al., 1998; Iribarren et al., 2009). The last of these basins' emersion was previously dated at 5.3 Ma, which indicates that the duration of tear propagation in the Betics (across 400 km distance) is 3–5 Myr. This assumption would give a tearing rate of 80–133 km/Myr. Nevertheless, more recent biostratigraphic studies by Krijgsman et al. (2018) and van der Schee et al. (2018) show that the timing of the uplift of the western Betic intramontane basins is still far from well determined, finding an age of 7.51 Ma (late Tortonian) for the latest preserved marine sediment in the Guadalhorce Basin. The new age constraint narrows down the plausible tear propagation duration to 1–3 Myr, which implies a faster tearing (133–400 km/Myr) rate than previously thought. Our tearing rate of 370-670 km/Myr, albeit very fast, still falls within the newly constrained tear propagation rate.

A limitation of our models lies in the lack of an arcuate slab so a full comparison cannot
be made with the interpreted 3D slab structure beneath the Gibraltar Arc System (Spakman
and Wortel, 2004; Chertova et al., 2014; Spakman et al., 2018). The uplift of intramountain basins within the Betics in southern Iberia is higher on the eastern side (Iribarren et al., 2009), where the slab is interpreted to be detached based on seismic tomography (Fig 9b). Such uplift is not detected in the western Betics where the tear point is and the part of the same slab still remains attached (Fig 9a). Our models predict a similar trend, with earlier and higher uplift on the eastern parts of the oblique margin (due to both continental-continental collision and slab tearing), and later and lower uplift in the west, where the slab still remain attached. The study of magnetostratigraphic sequences shows that the transition from marine to continental conditions of intramountain basins within the Betics is younging westward (Fig 1) (Garcés et al., 1998; Iribarren et al., 2009). This trend corresponds with our models' westward tear propagation, where the oldest uplifted region would be toward the east and the younger uplifted region toward the west.

Conclusion

We set out to investigate the slab tearing process, its dynamics, and its effect on surface topography using three-dimensional thermomechanical modelling. We used the Western Mediterranean as a reference scenario because the proposed tectonic reconstruction for the region involved slab tearing and its effect on the surface uplift.

Our results support the idea that the obliquity of the continental passive margin (relative to the trench axis) is a major influence on the initiation of slab tearing because it promotes a laterally diachronous continental convergence, which leads to slab tearing. This obliquity of the continental convergence produced an east-to-west slab tearing (tearing velocity 37.6–67.6 cm/yr with the lower-mantle viscosity of up to 10^{22} Pa $\cdot$s), which led to surface uplift signature of 0.5–1.5 km across the forearc region throughout the tearing process.

The slab tearing depth increases as it propagates along the slab, with a shallower tear (80–150 km) on the side where the tear initiated and a deeper tear (170–200 km) on the other side. The timing of the slab tearing in our models appears to be geologically fast (3 Myr). The key controls on the duration of detachment process are the viscosity of the sublithospheric mantle and the amount of shortening/oceanic subduction prior tearing (this affects how large and heavy the slab would be).

The uplift rate range produced by our model-setup, 0.23-2.16 mm/yr, is compatible with the uplift rates needed to achieve an equilibrium between seaway-uplift and seaway-erosion, which could have led to the closure of marine gateways that reduced the water-flow from the Atlantic Ocean into the Mediterranean Sea during the first stage of the Messinian Salinity Crisis

Acknowledgement

This work has been supported by EU Marie Curie Initial Training Network 'SUBITOP' (674899-SUBITOP-H2020-MSCA-ITN-2015), the Spanish Government national research program (GeoCAM, PGC2018-095154-B-I00) and the Generalitat de Catalunya grant (AGAUR 2017 SGR 847). We thank the Laboratorio de Geodinámica at GEO3BCN-CSIC as well as the Euler Cluster at the Scientific Computing centre at ETH Zürich for providing the computing facilities.

Author Contributions Statement

Kittiphon Boonma: Methodology, Software, Investigation, Formal analysis, Validation, Writing – Original Draft, Visualisation. **Daniel Garcia-Castellanos**: Conceptualisation, Resources, Funding acquisition, Supervision, Validation, and Writing – Review & Editing. **Ivone Jiménez-Munt**: Con-

ceptualisation, Resources, Funding acquisition, Supervision, Validation, and Writing – Review & Editing. **Taras Gerya**: Methodology, Software, and Writing – Review & Editing.

Data Availability Statement

The 3D numerical modelling code, I3ELVIS (Gerya, 2013) used in this study, which is a version implemented with grain-size reduction, is available from http://doi.org/10.5281/zenodo.4637879. The model setup codes are available from https://osf.io/j7gy6/ (Center for Open Science repository).

Declaration of competing interest

The authors declare no competing interests.

References

Andrews, E. R., & Billen, M. I. (2009). Rheologic controls on the dynamics of slab detachment. *Tectonophysics*, *464*(1–4), 60–69. https://doi.org/10.1016/j.tecto.2007.09.004Austermann, J., & Forte, A. M. (2019). The importance of dynamic topography for understanding past sea-level changes. *Past Global Changes Magazine*, *27*(1). https://doi.org/10.22498/pages.27.1.18Ávila, P., & Dávila, F. M. (2020). Lithospheric thinning and dynamic uplift effects during slab window formation, southern Patagonia. *Journal of Geodynamics*, *133*, 101689. https://doi.org/10.1016/j.jog.2019.101689Balázs, A., Faccenna, C., Ueda, K., Funiciello, F., Boutoux, A., Blanc, E. J. P., & Gerya, T. (2021). Oblique subduction and mantle flow control on upper plate deformation: 3D geodynamic modeling. *Earth and Planetary Science Letters*, *569*, 117056. https://doi.org/10.1016/j.epsl.2021.117056Billen, M. I. (2008). Modeling the dynamics of subducting slabs. *Annual Review of Earth and Planetary Sciences*, *36*, 325–356. https://doi.org/10.1146/annurev.earth.36.031207.124129Boonma, K., Kumar, A., Garcia-Castellanos, D., Jiménez-Munt, I., & Fernández, M. (2019). Lithospheric mantle buoyancy: the role of tectonic convergence and mantle composition. *Scientific Reports*, *9*(1), 17953. https://doi.org/10.1038/s41598-019-54374-wBoschi, L., Faccenna, C., & Becker, T. W. (2010). Mantle structure and dynamic topography in the Mediterranean Basin. *Geophysical Research Letters*, *37*(20), 20303. https://doi.org/10.1029/2010GL045001Burg, J. P., & Gerya, T. V. (2005). The role of viscous heating in Barrovian metamorphism of collisional orogens: Thermomechanical models and application to the Lepontine Dome in the Central Alps. *Journal of Metamorphic Geology*, *23*(2), 75–95. https://doi.org/10.1111/j.1525-1314.2005.00563.xCapella, W., Spakman, W., Hinsbergen, D. J. J., Chertova, M. V., & Krijgsman, W. (2020). Mantle resistance against Gibraltar slab dragging as a key

cause of the Messinian Salinity Crisis. *Terra Nova*, *32*(2), 141–150. https://doi.org/10.1111/ter.12442Carminati, E., Wortel, R., Spakman, W., & Sabadini, R. (1998). The role of slab detachment processes in the opening of the western–central Mediterranean basins: some geological and geophysical evidence. *Earth and Planetary Science Letters*, *160*(3–4), 651–665. https://doi.org/10.1016/S0012-821X(98)00118-6Chertova, M. V., Spakman, W., Geenen, T., van den Berg, A. P., & van Hinsbergen, D. J. J. (2014). Underpinning tectonic reconstructions of the western Mediterranean region with dynamic slab evolution from 3-D numerical modeling. *Journal of Geophysical Research: Solid Earth*, *119*(7), 5876–5902. https://doi.org/10.1002/2014JB011150Conrad, C. P., & Lithgow-Bertelloni, C. (2002). How mantle slabs drive plate tectonics. *Science*, *298*(5591), 207–209. https://doi.org/10.1126/science.1074161Coulson, S., Pico, T., Austermann, J., Powell, E., Moucha, R., & Mitrovica, J. X. (2019). The role of isostatic adjustment and gravitational effects on the dynamics of the Messinian salinity crisis. *Earth and Planetary Science Letters*, *525*, 115760. https://doi.org/10.1016/j.epsl.2019.115760Crameri, F., Schmeling, H., Golabek, G. J., Duretz, T., Orendt, R., Buiter, S. J. H. H., … Tackley, P. J. (2012). A comparison of numerical surface topography calculations in geodynamic modelling: an evaluation of the 'sticky air' method. *Geophysical Journal International*, *189*(1), 38–54. https://doi.org/10.1111/j.1365-246X.2012.05388.xDavies, J. H., & von Blanckenburg, F. (1995). Slab breakoff: A model of lithosphere detachment and its test in the magmatism and deformation of collisional orogens. *Earth and Planetary Science Letters*, *129*(1–4), 85–102. https://doi.org/10.1016/0012-821X(94)00237-Sde Lamotte, D. F., Leturmy, P., Missenard, Y., Khomsi, S., Ruiz, G., Saddiqi, O., … Michard, A. (2009). Mesozoic and Cenozoic vertical movements in the Atlas system (Algeria, Morocco, Tunisia): An overview. *Tectonophysics*, *475*(1), 9–28. https://doi.org/10.1016/j.tecto.2008.10.024Duretz, T., Gerya, T. V., & Spakman, W. (2014). Slab detachment in laterally varying subduction zones: 3-D numerical modeling. *Geophysical Research Letters*, *41*(6), 1951–1956. https://doi.org/10.1002/2014GL059472Duretz, Thibault, Gerya, T. V., & May, D. A. (2011). Numerical modelling of spontaneous slab breakoff and subsequent topographic response. *Tectonophysics*, *502*(1–2), 244–256. https://doi.org/10.1016/j.tecto.2010.05.024England, P., & Molnar, P. (1990). Surface uplift, uplift of rocks, and exhumation of rocks. *Geology*, *18*(12), 1173–1177. https://doi.org/10.1130/0091-7613(1990)018<1173:SUUORA>2.3.CO;2Faccenna, C., & Becker, T. W. (2010). Shaping mobile belts by small-scale convection. *Nature*, *465*(7298), 602–605. https://doi.org/10.1038/nature09064Faccenna, C., Becker, T. W., Miller, M. S., Serpelloni, E., & Willett, S. D. (2014). Isostasy, dynamic topography, and the elevation of the Apennines of Italy. *Earth and Planetary Science Letters*, *407*, 163–174. https://doi.org/10.1016/j.epsl.2014.09.027Faccenna, C., Bellier, O., Martinod, J., Piromallo, C., & Regard, V. (2006). Slab detachment beneath eastern Anatolia: A possible cause for the formation of the North Anatolian fault. *Earth and Planetary Science Letters*, *242*(1–2), 85–97. https://doi.org/10.1016/J.EPSL.2005.11.046Faccenna, C.,

Piromallo, C., Crespo-Blanc, A., Jolivet, L., & Rossetti, F. (2004). Lateral slab deformation and the origin of the western Mediterranean arcs. *Tectonics*, *23*(1), n/a-n/a. https://doi.org/10.1029/2002TC001488Forte, A. M., Peltier, W. R., Dziewonski, A. M., & Woodward, R. L. (1993). Dynamic surface topography: A new interpretation based upon mantle flow models derived from seismic tomography. *Geophysical Research Letters*, *20*(3), 225–228. https://doi.org/10.1029/93GL00249Fox, M., Herman, F., Kissling, E., & Willett, S. D. (2015). Rapid exhumation in the Western Alps driven by slab detachment and glacial erosion. *Geology*, *43*(5), 379–382. https://doi.org/10.1130/G36411.1Freeburn, R., Bouilhol, P., Maunder, B., Magni, V., van Hunen, J., Hunen, J. Van, & van Hunen, J. (2017). Numerical models of the magmatic processes induced by slab breakoff. *Earth and Planetary Science Letters*, *478*, 203–213. https://doi.org/10.1016/j.epsl.2017.09.008Garcés, M., Krijgsman, W., & Agustí, J. (1998). Chronology of the late Turolian deposits of the Fortuna basin (SE Spain): Implications for the Messinian evolution of the eastern Betics. *Earth and Planetary Science Letters*, *163*(1–4), 69–81. https://doi.org/10.1016/S0012-821X(98)00176-9Garcia-Castellanos, D., & Villaseñor, A. (2011). Messinian salinity crisis regulated by competing tectonics and erosion at the Gibraltar arc. *Nature*, *480*(7377), 359–363. https://doi.org/10.1038/nature10651Garcia-Castellanos, Daniel, Torne, M., & Fernàndez, M. (2000). Slab pull effects from a flexural analysis of the Tonga and Kermadec trenches (Pacific Plate). *Geophysical Journal International*, *141*(2), 479–484. https://doi.org/10.1046/j.1365-246X.2000.00096.xGarzanti, E., Radeff, G., & Malusà, M. G. (2018, February 1). Slab breakoff: A critical appraisal of a geological theory as applied in space and time. *Earth-Science Reviews*. Elsevier. https://doi.org/10.1016/j.earscirev.2017.11.012Gerya, Taras, & Yuen, D. (2003). Characteristics-based marker-in-cell method with conservative finite-differences schemes for modeling geological flows with strongly variable transport properties. *Physics of the Earth and Planetary Interiors*, *140*(4), 293–318. https://doi.org/10.1016/j.pepi.2003.09.006Gerya, Taras, & Yuen, D. (2007). Robust characteristics method for modelling multiphase visco-elasto-plastic thermo-mechanical problems. *Physics of the Earth and Planetary Interiors*, *163*(1–4), 83–105. https://doi.org/10.1016/j.pepi.2007.04.015Gerya, T. V., Perchuk, L. L., & Burg, J. P. (2008). Transient hot channels: Perpetrating and regurgitating ultrahigh-pressure, high-temperature crust-mantle associations in collision belts. *Lithos*, *103*(1–2), 236–256. https://doi.org/10.1016/j.lithos.2007.09.017Gerya, Taras V., Yuen, D. A., & Maresch, W. V. (2004). Thermomechanical modelling of slab detachment. *Earth and Planetary Science Letters*, *226*(1–2), 101–116. https://doi.org/10.1016/j.epsl.2004.07.022Gerya, Taras V. (2013). Three-dimensional thermomechanical modeling of oceanic spreading initiation and evolution. *Physics of the Earth and Planetary Interiors*, *214*, 35–52. https://doi.org/10.1016/j.pepi.2012.10.007Gvirtzman, Z., Faccenna, C., & Becker, T. W. (2016). Isostasy, flexure, and dynamic topography. *Tectonophysics*, *683*, 255–271. https://doi.org/10.1016/j.tecto.2016.05.041Harlow, F.

H., & Welch, J. E. (1965). Numerical Calculation of Time-Dependent Viscous Incompressible Flow of Fluid with Free Surface. *Physics of Fluids*, *8*(12), 2182. https://doi.org/10.1063/1.1761178Heller, P. L., & Liu, L. (2016). Dynamic topography and vertical motion of the U.S. Rocky Mountain region prior to and during the Laramide orogeny. *Bulletin of the Geological Society of America*, *128*(5–6), 973–988. https://doi.org/10.1130/B31431.1Hirth, G., & Kohlstedt, D. (2003). Rheology of the upper mantle and the mantle wedge: A view from the experimentalists (pp. 83–105). https://doi.org/10.1029/138GM06Iribarren, L., Vergés, J., & Fernàndez, M. (2009). Sediment supply from the Betic–Rif orogen to basins through Neogene. *Tectonophysics*, *475*(1), 68–84. https://doi.org/10.1016/j.tecto.2008.11.029Ito, E., Akaogi, M., Topor, L., & Navrotsky, A. (1990). Negative pressure-temperature slopes for reactions forming MgSiO 3 perovskite from calorimetry. *Science*, *249*(4974), 1275–1278. https://doi.org/10.1126/science.249.4974.1275Ito, K., & Kennedy, G. C. (1971). An Experimental Study of the Basalt-Garnet Granulite-Eclogite Transition. In J. G. Heacock (Ed.), *The Structure and Physical Properties of the Earth's Crust* (Vol. 14, pp. 303–314). American Geophysical Union (AGU). https://doi.org/10.1029/GM014p0303Jiménez-Munt, I., Torne, M., Fernàndez, M., Vergés, J., Kumar, A., Carballo, A., & García-Castellanos, D. (2019). Deep Seated Density Anomalies Across the Iberia-Africa Plate Boundary and Its Topographic Response. *Journal of Geophysical Research: Solid Earth*, *124*(12), 13310–13332. https://doi.org/10.1029/2019JB018445Jolivet, L., Faccenna, C., & Piromallo, C. (2009). From mantle to crust: Stretching the Mediterranean. *Earth and Planetary Science Letters*, *285*(1–2), 198–209. https://doi.org/10.1016/J.EPSL.2009.06.017Karato, S. -i. S. I., & Wu, P. (1993). Rheology of the upper mantle: A synthesis. *Science*, *260*(5109), 771–778. https://doi.org/10.1126/science.260.5109.771Katsura, T., & Ito, E. (1989). The system Mg 2 SiO 4 -Fe 2 SiO 4 at high pressures and temperatures: Precise determination of stabilities of olivine, modified spinel, and spinel. *Journal of Geophysical Research: Solid Earth*, *94*(B11), 15663–15670. https://doi.org/10.1029/JB094iB11p15663Katsura, T., Yoneda, A., Yamazaki, D., Yoshino, T., Ito, E., Suetsugu, D., … Jellinek, M. (2010). Adiabatic temperature profile in the mantle. *Physics of the Earth and Planetary Interiors*, *183*(1–2), 212–218. https://doi.org/10.1016/j.pepi.2010.07.001Krijgsman, W., Capella, W., Simon, D., Hilgen, F. J., Kouwenhoven, T. J., Meijer, P. T., … Flecker, R. (2018). The Gibraltar Corridor: Watergate of the Messinian Salinity Crisis. *Marine Geology*, *403*(June), 238–246. https://doi.org/10.1016/j.margeo.2018.06.008Kumar, A., Fernàndez, M., Vergés, J., Torne, M., & Jiménez-Munt, I. (2021). Opposite symmetry in the lithospheric structure of the Alboran and Algerian basins and their margins (Western Mediterranean): Geodynamic implications. *Journal of Geophysical Research: Solid Earth*, *126*(7). https://doi.org/10.1029/2020JB021388Li, Z. H., Xu, Z., Gerya, T., & Burg, J. P. (2013). Collision of continental corner from 3-D numerical modeling. *Earth and Planetary Science Letters*, *380*, 98–111. https://doi.org/10.1016/j.epsl.2013.08.034Liang, X., Chen, Y., Tian, X., Chen, Y. J., Ni, J., Gallegos, A., … Teng, J. (2016). 3D imaging of subducting and

fragmenting Indian continental lithosphere beneath southern and central Tibet using body-wave finite-frequency tomography. *Earth and Planetary Science Letters*, *443*, 162–175. https://doi.org/10.1016/J.EPSL.2016.03.029Lithgow-Bertelloni, C., & Silver, P. G. (1998). Dynamic topography, plate driving forces and the African superswell. *Nature*, *395*(6699), 269–272. https://doi.org/10.1038/26212Macchiavelli, C., Vergés, J., Schettino, A., Fernàndez, M., Turco, E., Casciello, E., … Tunini, L. (2017). A New Southern North Atlantic Isochron Map: Insights Into the Drift of the Iberian Plate Since the Late Cretaceous. *Journal of Geophysical Research: Solid Earth*, *122*(12), 9603–9626. https://doi.org/10.1002/2017JB014769Magni, V., Allen, M. B., van Hunen, J., Bouilhol, P., Hunen, J. Van, Bouilhol, P., … Bouilhol, P. (2017). Continental underplating after slab break-off. *Earth and Planetary Science Letters*, *474*, 59–67. https://doi.org/10.1016/j.epsl.2017.06.017Meulenkamp, J. E., Kováč, M., & Cicha, I. (1996). On Late Oligocene to Pliocene depocentre migrations and the evolution of the Carpathian-Pannonian system. *Tectonophysics*, *266*(1–4), 301–317. https://doi.org/10.1016/S0040-1951(96)00195-3Mitrofan, H., Anghelache, M. A., Chitea, F., Damian, A., Cadicheanu, N., & Vişan, M. (2016). Lateral detachment in progress within the Vrancea slab (Romania): Inferences from intermediate-depth seismicity patterns. *Geophysical Journal International*, *205*(2), 864–875. https://doi.org/10.1093/gji/ggv533Negredo, A. M., Mancilla, F. d. L., Clemente, C., Morales, J., & Fullea, J. (2020). Geodynamic Modeling of Edge-Delamination Driven by Subduction-Transform Edge Propagator Faults: The Westernmost Mediterranean Margin (Central Betic Orogen) Case Study. *Frontiers in Earth Science*, *8*, 6. https://doi.org/10.3389/feart.2020.533392Peral, M. (2020). *Dynamics of subduction Systems with opposite polarity in adjacent segments: application to the Westernmost Mediterranean.* Universitat de Barcelona.Ranalli, G. (1995). *Rheology of the Earth* (2nd ed.).Rosenbaum, G., Gasparon, M., Lucente, F. P., Peccerillo, A., & Miller, M. S. M. S. (2008). Kinematics of slab tear faults during subduction segmentation and implications for Italian magmatism. *Tectonics*, *27*(2). https://doi.org/10.1029/2007TC002143Rosenbaum, G., Lister, G. S., & Duboz, C. (2002a). Reconstruction of the tectonic evolution of the western Mediterranean since the Oligocene. *Journal of the Virtual Explorer*, *8*(January). https://doi.org/10.3809/jvirtex.2002.00053Rosenbaum, G., Lister, G. S., & Duboz, C. (2002b). Relative motions of Africa, Iberia and Europe during Alpine orogeny. *Tectonophysics*, *359*(1–2), 117–129. https://doi.org/10.1016/S0040-1951(02)00442-0Schellart, W. P. (2017). A geodynamic model of subduction evolution and slab detachment to explain Australian plate acceleration and deceleration during the latest Cretaceous-early Cenozoic. *Lithosphere*, *9*(6), 976–986. https://doi.org/10.1130/L675.1Schliffke, N., Hunen, J. van, Gueydan, F., Magni, V., & Allen, M. B. (2021). Curved orogenic belts, back-arc basins, and obduction asconsequences of collision at irregular continental margins. *Geology*. https://doi.org/10.1130/G48919.1Schmeling, H., Babeyko, A. Y., Enns, A., Faccenna, C., Funiciello, F., Gerya, T., … van Hunen, J. (2008). A benchmark comparison of spontaneous subduction models-Towards a free surface. *Physics of the Earth and Planetary Interiors*, *171*(1–4), 198–223.

https://doi.org/10.1016/j.pepi.2008.06.028Şengör, A. M. C., Özeren, S., Genç, T., & Zor, E. (2003). East Anatolian high plateau as a mantle-supported, north-south shortened domal structure. *Geophysical Research Letters*, *30*(24). https://doi.org/10.1029/2003GL017858Sinclair, H. D. (1997). Flysch to molasse transition in peripheral foreland basins: The role of the passive margin versus slab breakoff. *Geology*, *25*(12), 1123–1126. https://doi.org/10.1130/0091-7613(1997)025<1123:FTMTIP>2.3.CO;2Spakman, W, Wortel, M. J. R., & Vlaar, N. J. (1988). The Hellenic Subduction Zone: A tomographic image and its geodynamic implications. *Geophysical Research Letters*, *15*(1), 60–63. https://doi.org/10.1029/GL015i001p00060Spakman, Wim, Chertova, M. V., Van Den Berg, A., & van Hinsbergen, D. J. J. J. (2018). Puzzling features of western Mediterranean tectonics explained by slab dragging. *Nature Geoscience*, *11*(3), 211–216. https://doi.org/10.1038/s41561-018-0066-zSpakman, Wim, & Wortel, R. (2004). A Tomographic View on Western Mediterranean Geodynamics. In *The TRANSMED Atlas. The Mediterranean Region from Crust to Mantle* (pp. 31–52). Berlin, Heidelberg: Springer Berlin Heidelberg. https://doi.org/10.1007/978-3-642-18919-7_2Turcotte, D., & Schubert, G. (2014). *Geodynamics*. Cambridge University Press. https://doi.org/10.1017/CBO9780511843877Van Der Meulen, M. J., Meulenkamp, J. E., & Wortel, M. J. R. (1998). Lateral shifts of Apenninic foredeep depocentres reflecting detachment of subducted lithosphere. *Earth and Planetary Science Letters*, *154*(1–4), 203–219. https://doi.org/10.1016/s0012-821x(97)00166-0van der Schee, M., van den Berg, B. C. J., Capella, W., Simon, D., Sierro, F. J., & Krijgsman, W. (2018). New age constraints on the western Betic intramontane basins: A late Tortonian closure of the Guadalhorce Corridor? *Terra Nova*, *30*(5), 325–332. https://doi.org/10.1111/ter.12347Van Hinsbergen, D. J. J. J., Vissers, R. L. M. M., & Spakman, W. (2014). Origin and consequences of western Mediterranean subduction, rollback, and slab segmentation. *Tectonics*, *33*(4), 393–419. https://doi.org/10.1002/2013TC003349van Hinsbergen, D. J. J., Kaymakci, N., Spakman, W., & Torsvik, T. H. (2010). Reconciling the geological history of western Turkey with plate circuits and mantle tomography. *Earth and Planetary Science Letters*, *297*(3–4), 674–686. https://doi.org/10.1016/J.EPSL.2010.07.024van Hinsbergen, D. J. J., Lippert, P. C., Dupont-Nivet, G., McQuarrie, N., Doubrovine, P. V, Spakman, W., & Torsvik, T. H. (2012). Greater India Basin hypothesis and a two-stage Cenozoic collision between India and Asia. *Proceedings of the National Academy of Sciences of the United States of America*, *109*(20), 7659–7664. https://doi.org/10.1073/pnas.1117262109van Hunen, J., & Allen, M. B. (2011). Continental collision and slab break-off: A comparison of 3-D numerical models with observations. *Earth and Planetary Science Letters*, *302*(1–2), 27–37. https://doi.org/10.1016/j.epsl.2010.11.035Vergés, J., & Fernàndez, M. (2012). Tethys–Atlantic interaction along the Iberia–Africa plate boundary: The Betic–Rif orogenic system. *Tectonophysics*, *579*, 144–172. https://doi.org/10.1016/j.tecto.2012.08.032Wortel, M. J. R. (2000). Subduction and Slab Detachment in the Mediterranean-Carpathian Region. *Science*, *290*(5498), 1910–1917. https://doi.org/10.1126/science.290.5498.1910Wortel,

R., & Spakman, W. (1992). Structure and dynamics of subducted lithosphere in the Mediterranean region. In *Proc. Kon. Ned. Akad. v. Wetensch* (Vol. 95, pp. 325–347). Proc Kon Ned Akad v Wetensch.Wu, F.-Y., Ji, W.-Q., Wang, J.-G., Liu, C.-Z., Chung, S.-L., & Clift, P. D. (2014). Zircon U-Pb and Hf isotopic constraints on the onset time of India-Asia collision. *American Journal of Science*, *314*(2), 548–579. https://doi.org/10.2475/02.2014.04Yoshioka, S., & Wortel, R. (1995). Three-dimensional numerical modeling of detachment of subducted lithosphere. *Journal of Geophysical Research*, *100*(B10). https://doi.org/10.1029/94jb01258

1.

2.

Tables

Table 1 **Material properties used in the numerical experiments**. The flow law include: A is the pre-exponential factor; E denotes activation energy; V is activation volume; n is the stress exponent; m is grain size exponent; $_{cr}$ is critical stress or the the assumed diffusion-dislocation transition stress; C is the rock compressive strength at P=0 MPa; $_{0}$ and $_{1}$ are the initial and final internal coefficients, respectively parameters (Karato and Wu, 1993; Ranalli, 1995; Hirth and Kohlstedt, 2003; Turcotte and Schubert, 2014). The subscripts 'diff' and 'disl' indicate that those parameters are associated with diffusion and dislocation creep processes, respectively. Mod3 has higher values for mantle activation volume than other models. Mod4 has higher final internal friction coefficient for lower oceanic crust and the mantle. Other properties for all rock types include: heat capacity C_p = 1000 J/(kg · K), thermal expansion = 2×10^{-5} 1/K; and compressibility = 6×10^{-12} 1/Pa.

Material	**Density** $_{0}$ **(kg/m^3)**	
(W/m · K)	**Flow Law**	**Flow law parameters**

Upper continental crust (Felsic)	$+807/(T+77)$	Wet quartzite (Ranalli, 1995)	A $=1.97\times10^{17}$ Pa^{n}s, n=2.3, E=1.54×10^5 J/mol, V=0 J/(mol $\cdot$ MPa), $_{cr}$=3×10^4 Pa, C=3 MPa, $_0$=0.3, $_1$=0
Lower continental crust (Gabbro)	$+474/(T+77)$	Plagioclase An75 (Ranalli, 1995)	A $=4.80\times10^{22}$ Pa^{n}s, n=3.2, E=2.38×10^5 J/mol, V=0 J/(mol $\cdot$ MPa), $_{cr}$=3×10^4 Pa, C=3 MPa, $_0$=0.3, $_1$=0
Upper oceanic crust (Basalt)		Wet quartzite (Ranalli, 1995)	A $=4.80\times10^{22}$ Pa^{n}s, n=3.2, E=2.38×10^5 J/mol, V=0 J/(mol $\cdot$ MPa), $_{cr}$=3×10^4 Pa, C=3 MPa, $_0$=0, $_1$=0
Lower oceanic crust (Gabbro)		Plagioclase An75 (Ranalli, 1995)	A $=4.80\times10^{22}$ Pa^{n}s, n=3.2, E=2.38×10^5 J/mol, V=0 J/(mol $\cdot$ MPa), $_{cr}$=3×10^4 Pa, C=3 MPa, $_0$=0.6, $_1$=0.0 **Mod4**: $_1$=0.3

Mantle	$+1293/(T+77)$ $\times\exp(0.000004P)$	Dry olivine (Hirth & Kohlstedt, 2003)	m=3, A_{diff} =1.50×10^{15} Pa s, E_{diff}=3.75×10^5 J/mol, V_{diff}=0.7 J/(mol · MPa), A_{disl} =1.10×10^{16} Pa^{n}s, n=3.5, E_{disl}=5.30×10^5 J/mol, V_{disl}=2.6 J/(mol · MPa), C=3 MPa, $_0$=0.6, $_1$=0.0 **Mod3**: V_{diff}=0.8 J/(mol · MPa), V_{disl}=3.0 J/(mol · MPa) **Mod4**: $_1$=0.3
Mantle weak zone			m=3, A_{diff} =1.50×10^{15} Pa s, E_{diff}=3.75×10^5 J/mol, V_{diff}=0.7 J/(mol · MPa), A_{disl} =1.10×10^{16} Pa^{n}s, n=3.5, E_{disl}=5.30×10^5 J/mol, V_{disl}=2.6 J/(mol · MPa), C=3 MPa, $_0$=0, $_1$=0

Table 2 **Model list**.

Model	Description	Incoming Continent	Slab detachment	Slab tear p
Mod1	Reference model	Yes	Yes	42.6
Mod2	No incoming continental block	No	Yes	67.6
Mod3	Higher ductile viscosity of the mantle	Yes	Yes	37.6
Mod4	Higher brittle strength of the mantle	Yes	No	-
Mod5	Fixed the convergence velocity	Yes	No	-

Figures

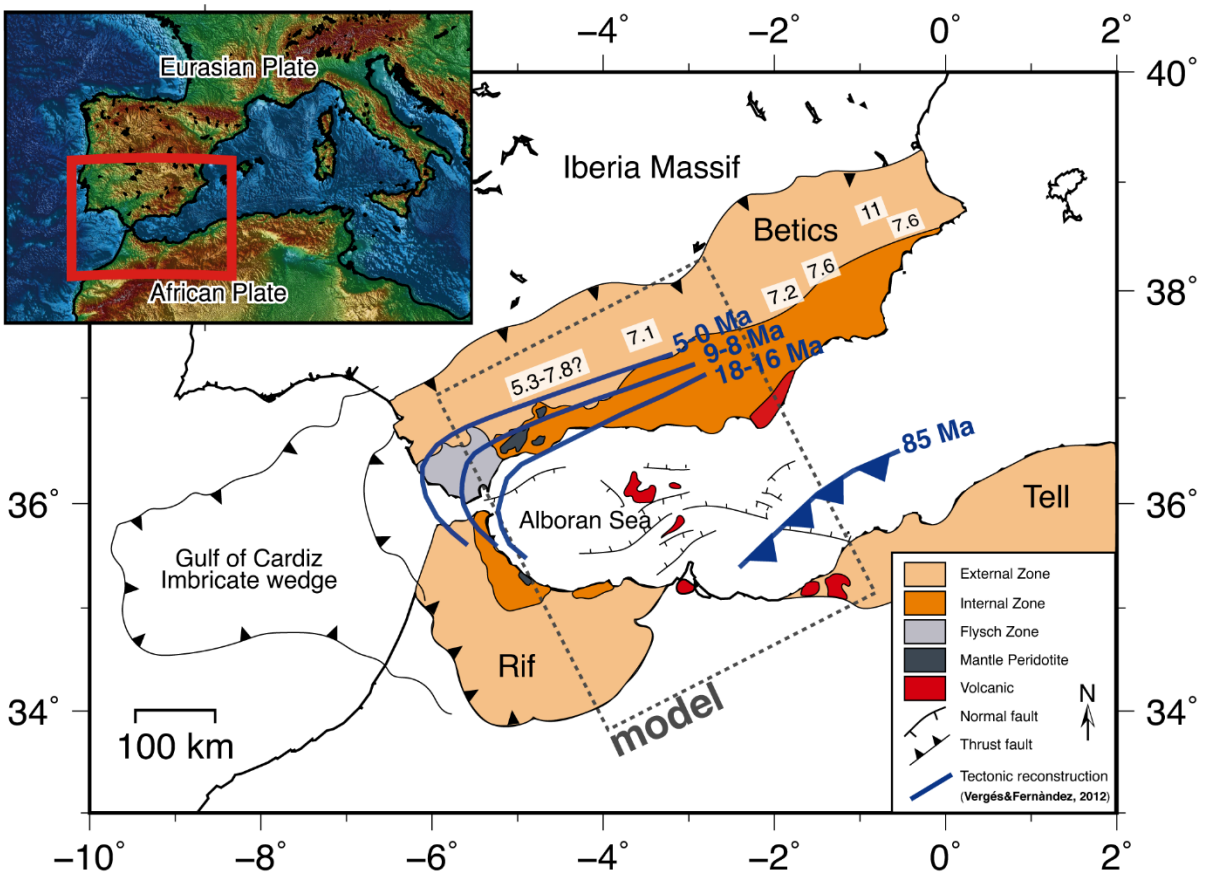

Fig 1. **Gibraltar Arc region**. A present-day schematic map of the Gibraltar Arc System (Western Mediterranean Sea; after Rosenbaum et al., 2002a), on which our model set up is based. The inset is a topography-bathymetry map, with our region of interest in the red box. The map displays key units of the Gibraltar Arc System: External Zone, Internal Zone, and the Flysch Zone (Suture Zone). The blue lines are the reconstruction of the Ligurian-Tethys

domain between Iberia and Africa (Late Cretaceous) before the onset of the African convergence, as proposed by Vergés and Fernàndez (2012). The grey frame outlines the area and the basic features therein, which the model setup is based on. The model frame is at such angle to encapsulate the stages from the reconstruction that involve slab detachment i.e. from 18–0 Ma. The numbers in white rectangles are the ages in Ma of the transition from marine to continental conditions of intramountain basins within the Betics (Iribarren et al., 2009; Krijgsman et al., 2018; van der Schee et al., 2018).

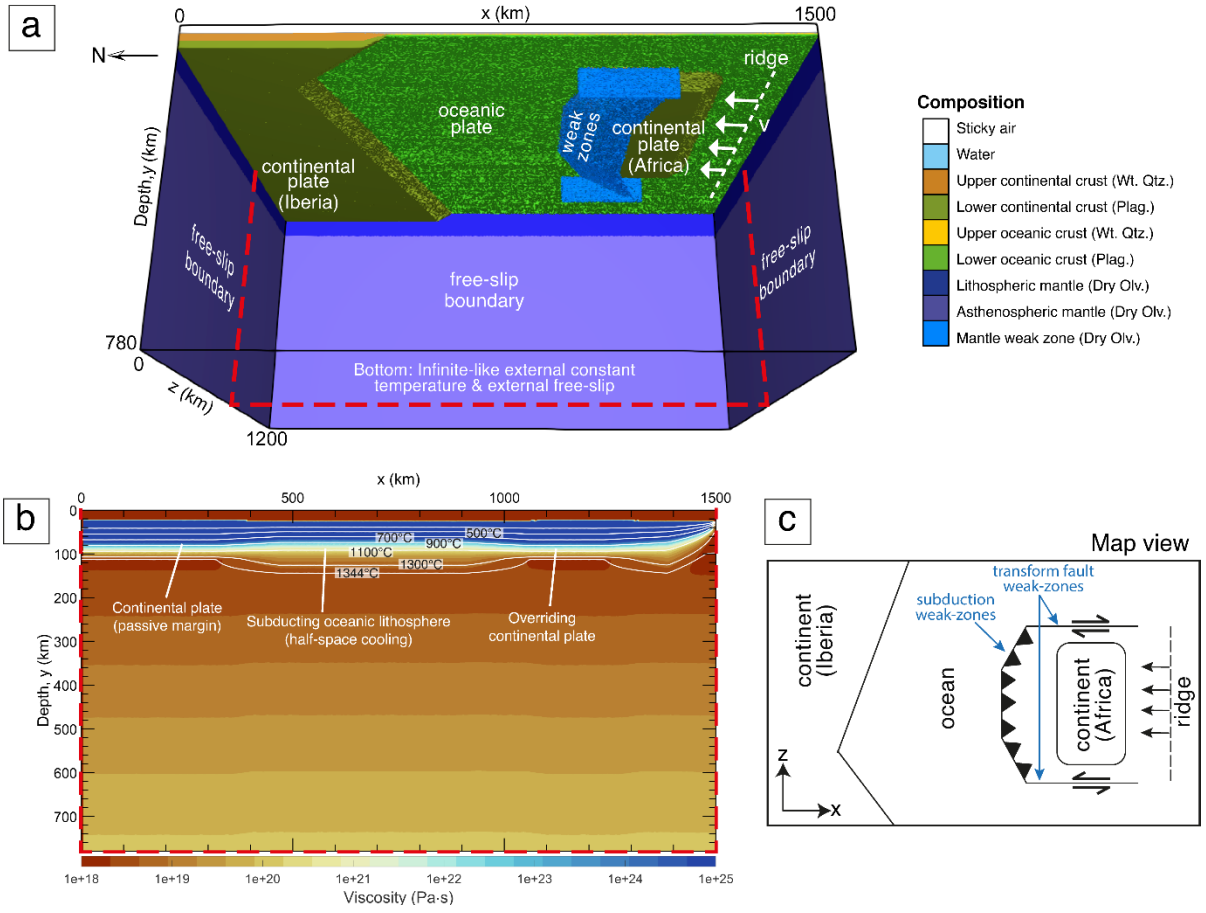

Fig 2. **Setup of Mod1-reference model**. a) 3D model domain (1500 × 780 × 1200 km) with colours representing different compositions. The flow law abbreviations are Wt Qtz. – wet quartzite; Plag. –Plagioclase; and Dry Olv. – Dry Olivine. Convergence is imposed by applying a uniform velocity (v) of 47

mm yr^{-1} until the slab reaches 200 km depth, after which v is either controlled by the sinking slab or reduced to another constant velocity. b) A cross-section profile of the viscosity. c) A map view of the model.

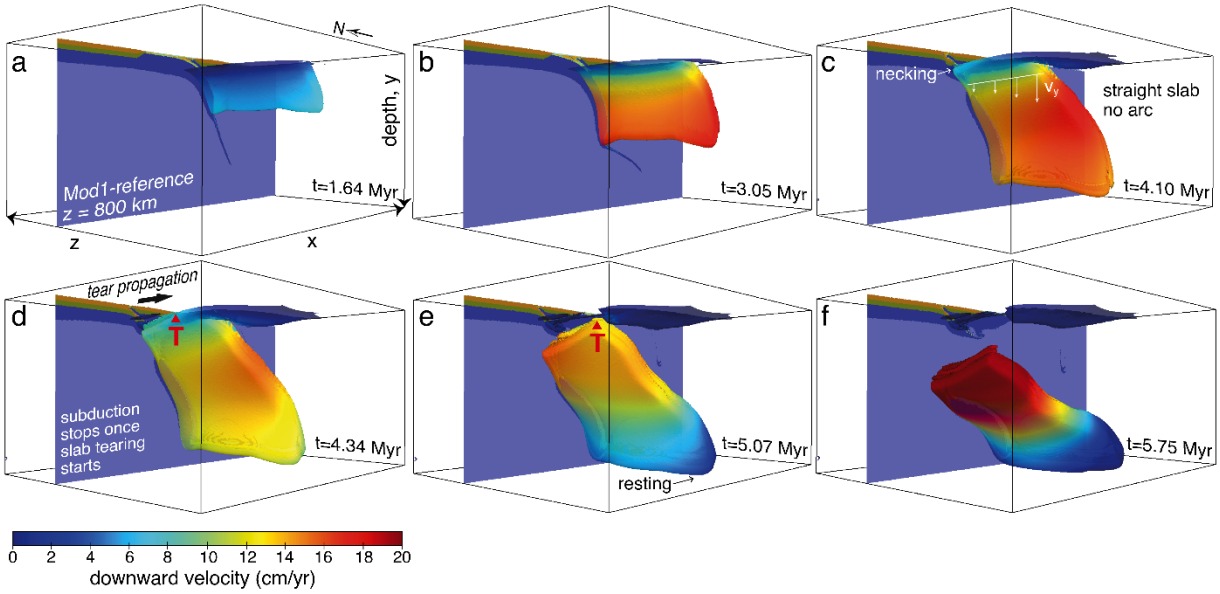

Fig 3. **The evolution of the slab's downward velocity (Mod1-reference)**. The slab structure shown here comes from the temperature isosurface, T=1300°C. The cross-section (z=800 km) shows the lithology/composition (for rock composition colour legends please refer to Fig 2. The red 'T' illustrates the position of the slab tear. Prior necking or slab tearing, the slab subducts with little lateral velocity variation across the slab (a and b). Once the necking and the tearing has started, the higher downward velocity now shifted to side of the slab that is still attached (c and d). After the slab is completely detached (f), the slab's downward velocity regained the lateral uniformity of downward velocity.

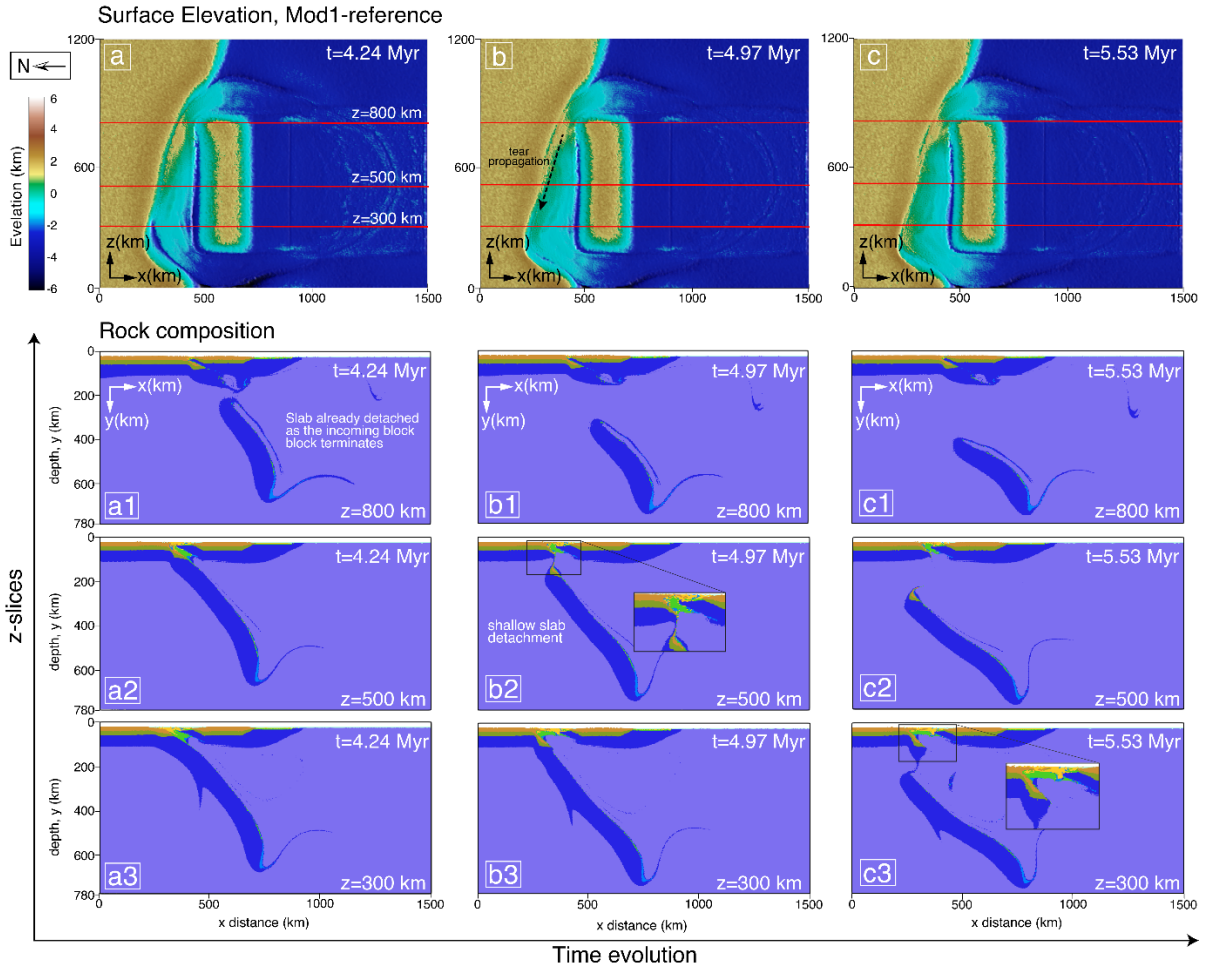

Fig 4. **Evolution of the reference model** (Mod1-reference) shown as surface topography (a, b, and c) and lithology (a1-3, b1-3, and c1-3). The colour coding for the lithology slices is the same as in Fig 2. Set (a) show the stage at which the continental-continental collision causes the incoming continental block to stop completely. The slab has already started to detach on the eastern side (z=800 km) by this point. In Set (b), the slab is half-torn with the attached portion of the slab still exerting slab-pull force. In Set (c), the tearing is approaching the western most side of the slab. Here the tearing/pinching occur at a deeper depth as the slab was still sinking until the arrival of the tearing. The tearing propagates westward as exhibited in a1, b2, and c3 cross-sections.

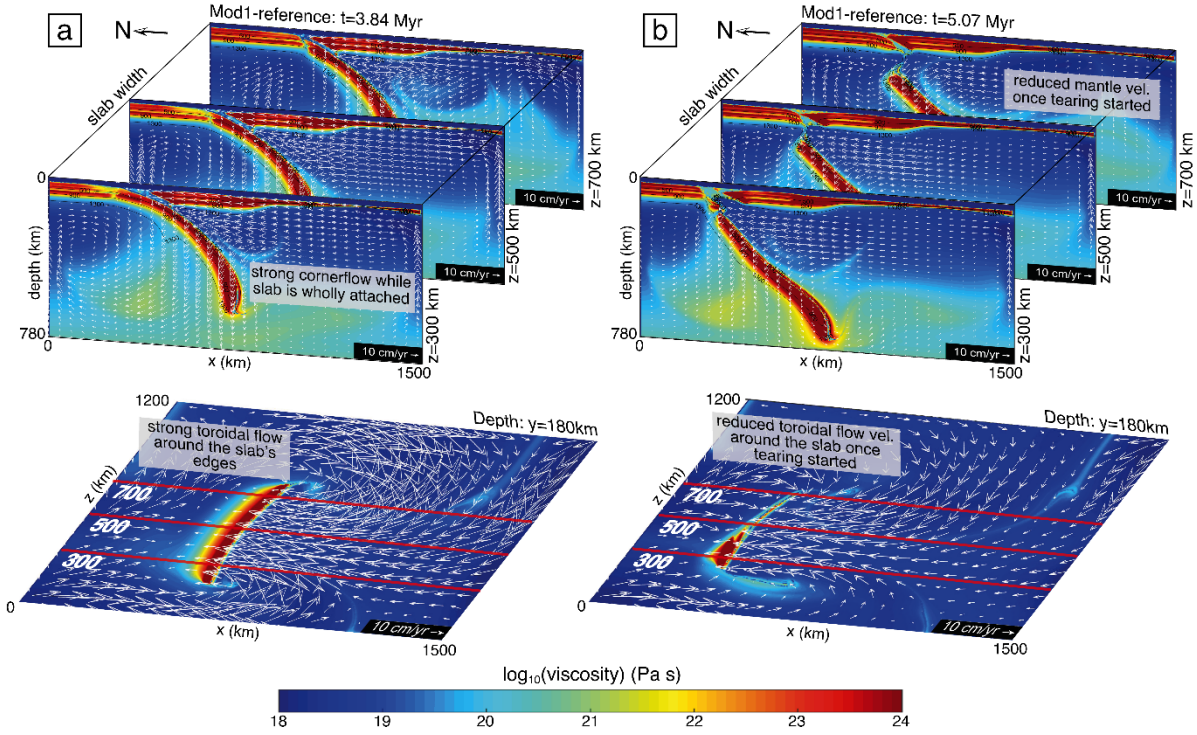

Fig 5 **Reference model viscosity cross-sections with velocity fields**. The upper panels shows the x-y cross-sections from z=300, 500, and 700 km, while the bottom panels shows the x-z cross-sections from the depth y=180 km, and the red lines correspond to the x-y slices in the panel above. The cross-sections in (a) come from a stage when the lithospheric slab is still wholly attached. The large hanging slab disturbs the mantle flow and causes mantle corner flow to build up, as well as causing strong mantle flow around the slab. The cross-sections in (b) are from the stage after slab tearing has started (on the eastern side). The mantle flow velocity is reduced as the slab-tear window allows the mantle to flow through.

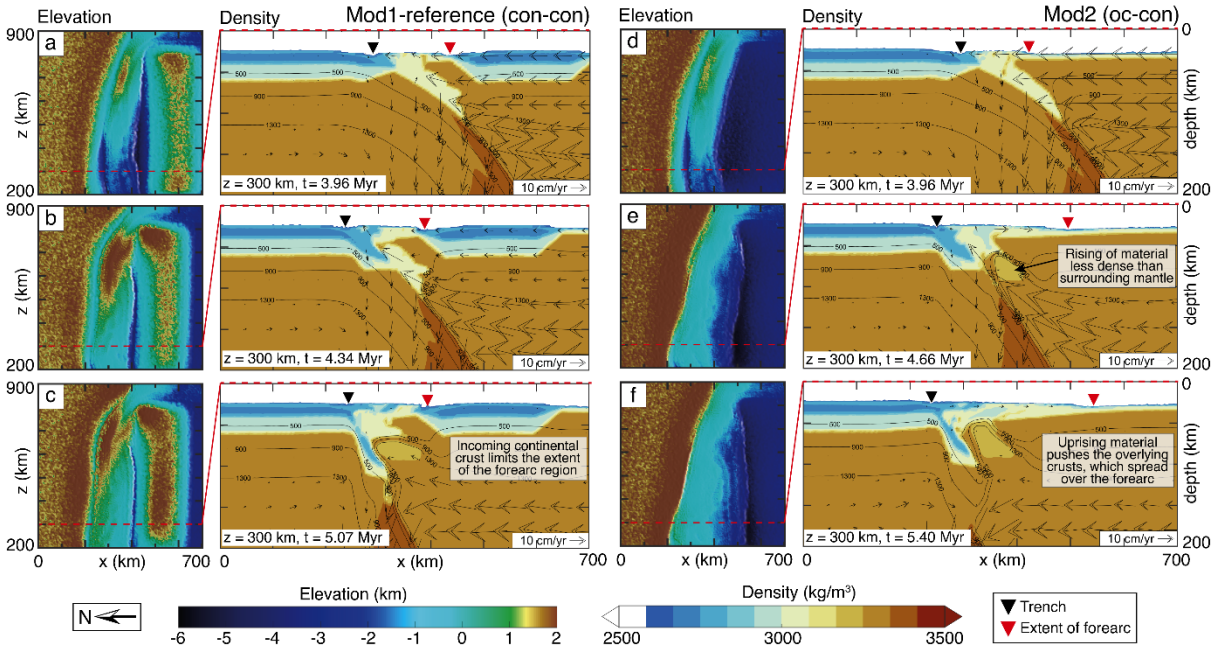

Fig 6 **The incoming continental crust limits the extent of forearc**. Shown here are elevation and density plots of model Mod1-reference (a, b, c) and Mod2 (d, e, f). The density cross-sections are taken from z = 300 km, shown as a red dashed line on each corresponding elevation plot. The black triangle indicates the position of the trench and the red triangle indicates the extent of the forearc. In both models, a body of less density (3200 kg/m^3) than the surrounding mantle exhumes up the subduction channel (c, e, f). The exhumed material thrusts under the overlying crust leading to a raised elevation. In Mod1-reference, the buoyant incoming continental crust (right, southern side of the model) limits the extent of the forearc region to the area in-between the passive margin and the incoming continental crust. In Mod2, the lack of a buoyant continental crust allows the crustal material, which are pushed up by mantle exhumation, to spread over a wider area and extending the forearc region.

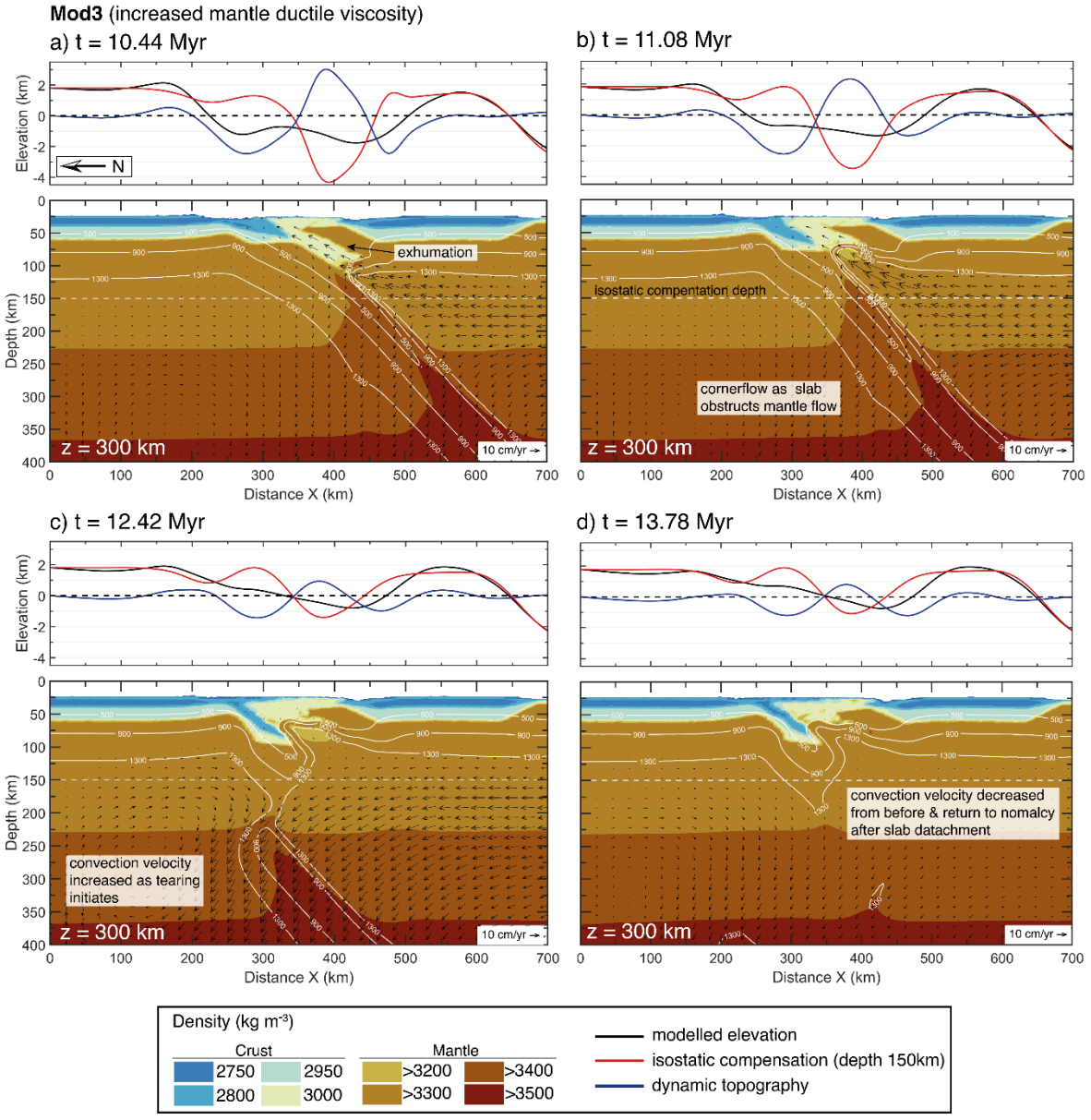

Fig 7. **Dynamic topography and density for model Mod3 (higher ductile viscosity of the mantle)**. The elevation plots (top panels) consist of: (i) total elevation resulting from the model (black); (ii) component of elevation corresponding to isostatic compensation of the crust (red); and (iii) component related to dynamic topography (blue). The isostatic effect was calculated with a compensation depth of 150 km (~128 km below crustal surface). The density (kg/m^3) distribution (bottom panels) is overlaid with temperature contours of

the lithospheric mantle (500°C, 900°C, and 1300°C). (a) From the stage when the incoming continental block came to a complete stop. (b) Pre-detachment stage with ongoing exhumation of the subducted oceanic crust and corner flow as the slab obstructs mantle flow. (c) During necking and tearing when mantle flow focus on the detaching slab and decrease the convection velocity in the upper part of the mantle. (d) Post-detachment stage when the mantle flow returns to its unperturbed state and convection velocity are reduced (the detached slab is at 450–660 km depth).

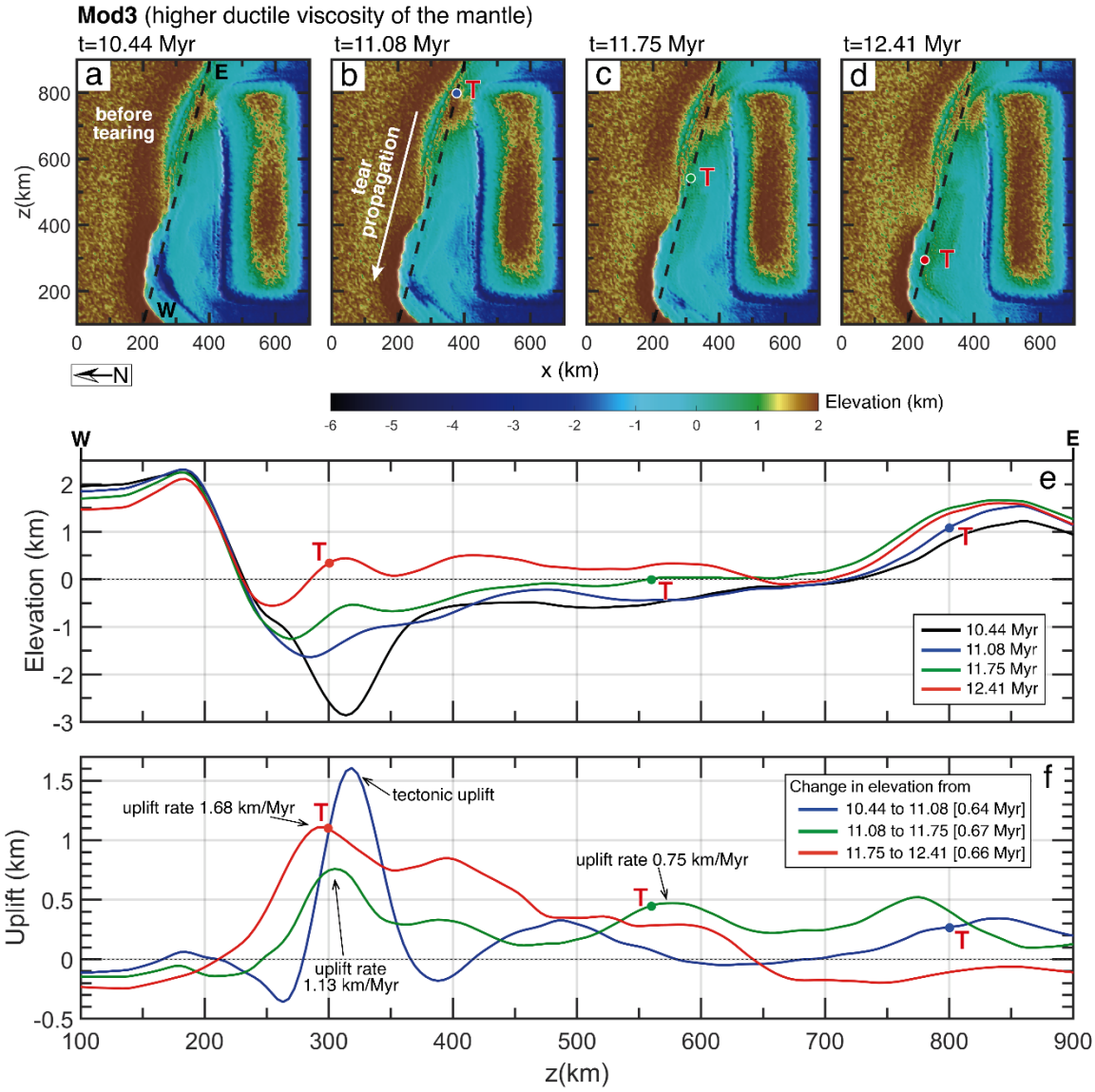

Fig 8. **Elevation evolution of model Mod3 (higher ductile viscosity of the mantle)**. (a), (b), (c), and (d) are map views of the model's surface elevation evolution with the tear propagating westward. The red 'T' indicates the slab-tear position in the subsurface. The dash lines (W-E) in (a) through (d) represent the elevation profiles shown in plot (e). Plot (f) shows the amount of uplift between time steps as the tearing propagates westward. The elevation increases as the tear propagates, with the maximum uplift rate of 1.68 km/Myr in the west. As the tear moves westward, the region toward the east of the profile W-E starts to subside, as shown with the red line in plot (e).

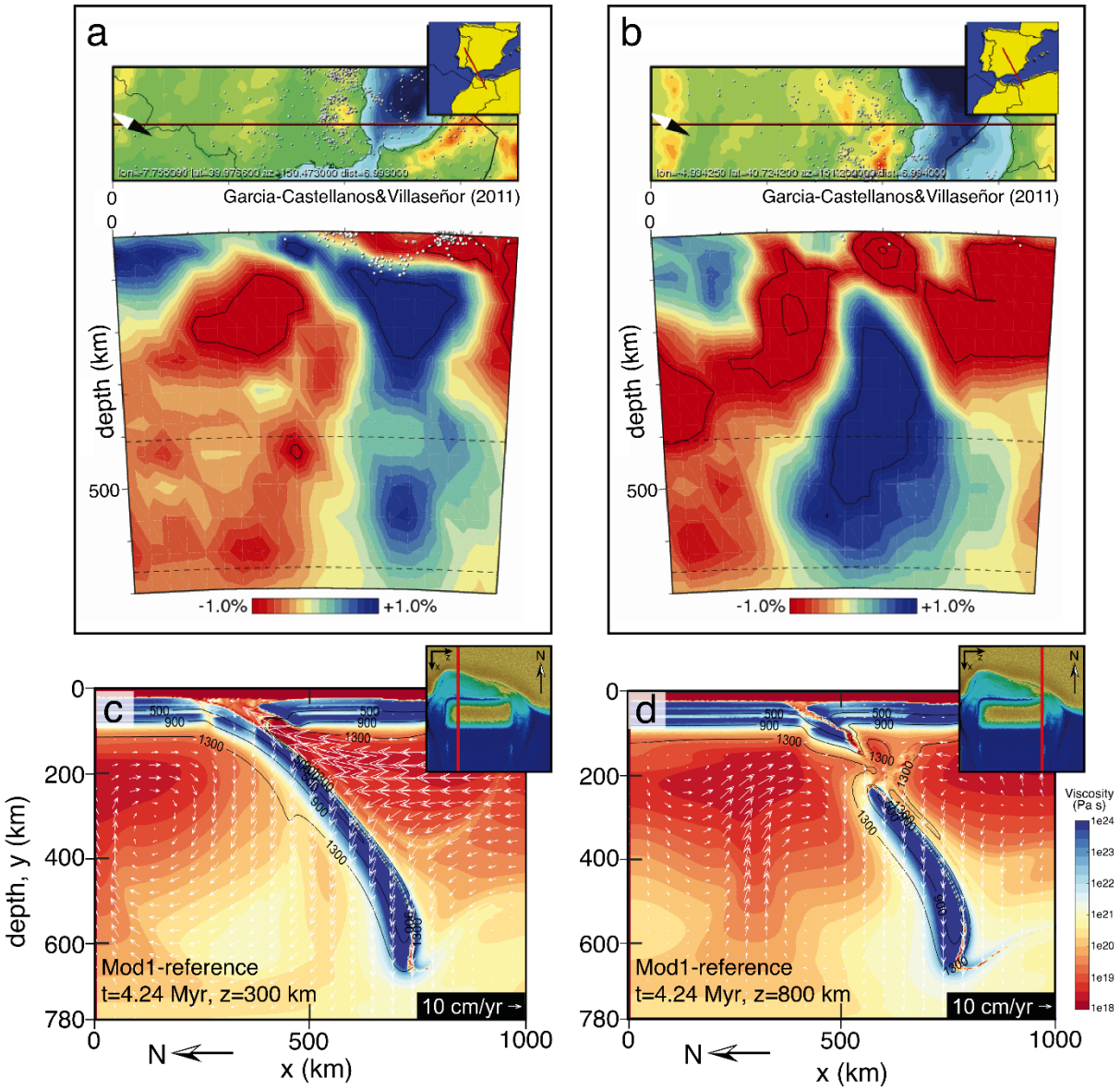

Fig 9. **Comparison of slab structure from Mod1-reference with the seismic tomography of the Western Mediterranean**. (a) and (b) are seismic tomographic images from Garcia-Castellanos & Villaseñor (2011) showing the distribution of fast- (blue) and slow-seismic-velocity (red). (c) and (d) are viscosity cross-sections from model Mod1-reference with (c) sliced from z=300 km, where the subducting slab is still attached and (d) sliced from z=800 km, where the slab has just started tearing. The subsets in (c) and (d) show the plan-view (x-z) of the surface elevation, and the red lines indicate the position

of the corresponding cross-sections. The cross-sections from Mod1-reference resemble, to an extent, the seismic tomography from the Western Mediterranean, with the attached portion of the slab on the NW side (a) and the detached slab toward the NE side (b).